# Vertical Structure and Microphysical Characteristics of Frontal Systems Passing over a Three-Dimensional Coastal Mountain Range

JOSEPH P. ZAGRODNIK AND LYNN A. MCMURDIE

*University of Washington, Seattle, Washington*

ROBERT A. HOUZE JR.

*University of Washington, Seattle, and Pacific Northwest National Laboratory, Richland, Washington*

SIMONE TANELLI

*Jet Propulsion Laboratory, California Institute of Technology, Pasadena, California*

(Manuscript received 14 September 2018, in final form 27 February 2019)

ABSTRACT

As midlatitude cyclones pass over a coastal mountain range, the processes producing their clouds and precipitation are modified, leading to considerable spatial variability in precipitation amount and composition. Statistical diagrams of airborne precipitation radar transects, surface precipitation measurements, and particle size distributions are examined from nine cases observed during the Olympic Mountains Experiment (OLYMPEX). Although the pattern of windward enhancement and leeside diminishment of precipitation was omnipresent, the degree of modulation was largely controlled by the synoptic environment associated with the prefrontal, warm, and postfrontal sectors of midlatitude cyclones. Prefrontal sectors contained homogeneous stratiform precipitation with a slightly enhanced ice layer on the windward slopes and rapid diminishment to a near-complete rain shadow in the lee. Warm sectors contained deep, intense enhancement over both the windward slopes and high terrain and less prominent rain shadows owing to downstream spillover of ice particles generated over terrain. Surface particle size distributions in the warm sector contained a broad spectrum of sizes and concentrations of raindrops on the lower windward side where high precipitation rates were achieved from varying degrees of both liquid and ice precipitation-generating processes. Spillover precipitation was rather homogeneous in nature and lacked the undulations in particle size and concentration that occurred at the windward sites. Postfrontal precipitation transitioned from isolated convective cells over ocean to a shallow, mixed convective–stratiform composition with broader coverage and greater precipitation rates over the sloping terrain.

## 1. Introduction

Precipitation over midlatitude West Coastal mountain ranges is usually associated with baroclinic frontal cyclones containing distinct cloud patterns, which are modified during passage over complex terrain (Nagle and Serebreny 1962; Medina et al. 2007). Observations from numerous past field programs have characterized the complex ways in which warm processes (condensation/collision–coalescence) and cold processes (riming, accretion, and aggregation) contribute to the modification of precipitation processes over West Coastal mountains (e.g., Anders et al. 2007; Hobbs et al. 1971; Houze et al. 1976; Hobbs 1978; Matejka et al. 1980; Bond et al. 1997; Ralph et al. 1999; Stoelinga et al. 2003; Houze and Medina 2005; Medina et al. 2007; Minder et al. 2008; Barrett et al. 2009; Viale et al. 2013; Massmann et al. 2017; Zagrodnik et al. 2018). Ground-based scanning radars have been especially valuable in determining the specific processes that lead to modification of precipitation but have tended to emphasize the windward side because of the hydrologic impacts caused by heavy precipitation. Models are able to simulate the diminishing precipitation over the high terrain and in regions of leeside descent (e.g., Colle 2004; Zängl 2005;

Denotes content that is immediately available upon publication as open access.

*Corresponding author*: Joseph P. Zagrodnik, jzagrod@uw.edu

DOI: 10.1175/JAS-D-18-0279.1

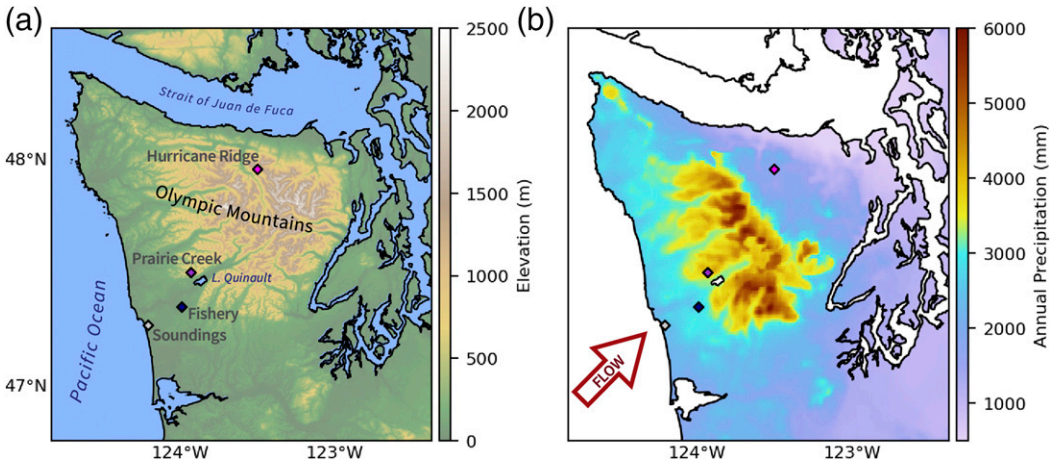


FIG. 1. Terrain and annual precipitation of the Olympic Peninsula: (a) topographic map and (b) estimated annual precipitation (mm) from the PRISM model (Daly et al. 2008) over the 1981–2010 time period. Disdrometer and sounding site locations used in this study are indicated with diamonds in both panels and labeled in (a).

Picard and Mass 2017). However, model accuracy is difficult to evaluate because of a dearth of observations of high-terrain and leeside precipitation processes. Surface and radar observations made from ground sites near mountain ranges are often limited by inaccessibility, terrain blockage, and beam widening.

To better understand the mechanisms controlling the precipitation across midlatitude coastal mountain ranges, the 2015/16 Olympic Mountains Experiment (OLYMPEX; Houze et al. 2017) deployed numerous observational resources across the windward, interior, and lee sides of the Olympic Mountains, where the climatological windward side experiences thousands of millimeters of precipitation and the lee side is very dry (Fig. 1). In a recent study using OLYMPEX data, Purnell and Kirshbaum (2018, hereafter PK18) used rain gauges and operational National Weather Service radars to show that orographic precipitation distributions are highly sensitive to the upstream static stability, horizontal moisture flux, and the presence of preexisting precipitation associated with the large-scale synoptic storm sectors. McMurdie et al. (2018) found that when the large-scale conditions resembled warm sectors (moist-neutral upstream stability combined with high horizontal water vapor flux), the precipitating cloud over terrain was enhanced in the ice layer throughout the depth of the precipitating system. Zagrodnik et al. (2018) showed that the periods of heaviest rainfall on the windward slopes often contained large concentrations of small drops, suggesting that warm precipitation processes are dominant during the strongest terrain-induced enhancement. Based on quasi-idealized model simulations, PK18 argued that at least some preexisting precipitation was required to fully realize the observed windward-side precipitation enhancement. However, it remains unclear how windward-side precipitation enhancement rates are controlled by the simultaneous variability of both warm and ice precipitation processes.

Precipitation reaching the lee side can be modified by synoptic and dynamic mechanisms associated with frontal cyclones. Mass et al. (2015) and Siler and Durran (2016) investigated the reasons for weak and strong rain shadows in the lee of the quasi-linear (two-dimensional), north–south-oriented Washington Cascades. From a synoptic viewpoint, both studies showed that weaker rain shadows on the eastern slopes were favored in the prefrontal (warm frontal) periods of midlatitude cyclone passages, prior to the erosion of the preexisting stable air mass in the lee. Siler and Durran (2016) found that weaker rain shadows were associated with muted lee-wave activity, a consequence of low-level cold, stagnant air disfavoring descent in the lee. Mass et al. (2015) suggested a different mechanism for weak-rain-shadow scenarios: southeasterly upslope flow on the eastern slopes induced by the approaching frontal trough. In contrast, PK18 found the strongest rain shadows in prefrontal periods over the circular, quasi-dome-shaped (three-dimensional) Olympic Mountains due to strong leeside mountain-wave descent favored by a statically stable upstream environment. Cold, stagnant air in the lee of a dome-shaped mountain range is more easily eroded by low-level air flowing around the barrier (Mass and Ferber 1990; Colle and Mass 1996), possibly explaining the difference in leeside behavior in the two types of mountain ranges. In addition to dynamical effects, liquid- and ice-phase microphysical growth rates may determine if particles

grow fast enough to fall out on the windward site or are advected to the lee side (Hobbs et al. 1973).

Surface disdrometer and airborne radar observations from OLYMPEX offer an opportunity to carefully examine the microphysical processes associated with the modification of precipitation over full transects of a coastal dome-shaped mountain range. These observations form the foundation of this study, which addresses the following two questions:

1) What large-scale environmental and microphysical processes control the enhancement of precipitation on the windward side and the diminishment of precipitation on the high terrain and lee side of a three-dimensional coastal mountain range?
2) How does the composition, size, and concentration of liquid and frozen precipitation particles vary as a function of the enhancement and diminishment characteristics?

## 2. Data

This study uses several observational assets including precipitation rate and particle size distributions from ground-based instrumentation, and airborne radar data collected during nine separate flight missions during OLYMPEX. Details of each of these platforms are described below.

### *a. Airborne Precipitation and Cloud Radar Third Generation*

The onboard instruments of the National Aeronautics and Space Administration (NASA) DC-8 aircraft used in OLYMPEX simulated the measurements that are made aboard the GPM *Core Observatory* satellite (Skofronick-Jackson et al. 2017), including the Airborne Precipitation and Cloud Radar Third Generation (APR-3). The DC-8 flew at altitudes of 10–11 km with the APR-3 obtaining measurements of reflectivity at Ku (13.4 GHz), Ka (35.6 GHz), and W (94.9 GHz) bands. The antenna scanned cross-track ±25° with 30-m range sampling. The Ku-band radar reflectivity factor is used in this study, as it is sufficient to capture the salient features of the storm structure and occurrence of precipitation. The footprint was approximately 0.8 km for a 10-km flight altitude. The sensitivity of the Ku band is 0 dB$Z$ at 5-km distance and the calibration uncertainty is ±1.5 dB. To mitigate the effects of aircraft roll, only the beam closest to nadir in each scan is used in this study.

The original APR-3 data obtained from the Distributed Active Archive Centers (DAAC; Durden and Tanelli 2018) were further processed by first cleaning the data and removing all of the ground clutter while retaining as much near-surface data as possible. In the current version of the Ku reflectivity product, isolated spikes of 10–15-dB$Z$ reflectivity within broader regions of weak reflectivity frequently affect low signal-to-noise (SNR) regions. A 2D Gaussian filter with a standard deviation of 1.5 bins (R. Chase 2018, personal communication) effectively removed the speckling without degrading the reflectivity information, as seen in the example transects provided in section 3. We also removed all Ku data where the cleaner and more sensitive Ka-band reflectivity was less than 0 dB$Z$.

The surface clutter removal involves several steps. Over regions of steep terrain, the radar beam partially intersects the land surface, leading to considerable variation in the number of bins with clutter above the estimated surface height. When the radar bright band intersects with terrain, it often mimics the decrease in reflectivity with height associated with ground clutter. Because of these complicating factors, we first generated an a priori estimate of the lowest clutter-free bin in each APR-3 profile using a surface roughness parameter defined by the standard deviation of the top of strongest ground clutter (>50 dB$Z$) associated with the ground surface over a five-footprint moving range in the horizontal. Our algorithm then removes the region above the APR-3 surface flag with decreasing reflectivity with height (<−0.1 dB per bin) within the height window predicted by the surface roughness estimate. At least 10 bins (300 m) are removed from every profile with up to 20 bins (600 m) removed in steep mountainous terrain. Visual inspection of all flight legs confirms the effectiveness of this method at removing all clutter, although it does occasionally remove a few more bins than necessary to safely ensure that all surface clutter is removed.

The accepted reflectivity data were compiled into two types of diagrams: contoured frequency by altitude diagrams (CFADs; Yuter and Houze 1995) and gridded maps of reflectivity height and coverage. The CFADs were constructed by binning the quality-controlled Ku reflectivity data into two-dimensional histograms of reflectivity from 0 to 50 dB$Z$ in 1-dB intervals between heights above sea level of 1.5 and 8.0 km in 0.25-km intervals. Each CFAD is normalized by the maximum bin at any level after correcting the sample size for terrain obstruction at lower levels. The terrain correction primarily affects the four lowest bins (1.5–2.5 km) in the high-terrain region, where the ground clutter obstructs 77%, 57%, 46%, and 16% of the sample, respectively. The resultant CFADs have values ranging from 0% to 100% at each 0.25-km height interval. Difference CFADs were also generated by subtracting the ocean

CFAD from the coast, windward, high-terrain, and leeside CFADs. Compared with the normalization-by-level methodology employed in McMurdie et al. (2018) where each height level is an independent sample, normalizing by the overall maximum bin allows for examination of the relative difference in frequency between various heights. The CFAD heights are relative to sea level and are not adjusted for brightband height.

In addition to the CFADs, gridded maps of Ku 15-dB$Z$ echo-top height and frequency are included to supplement the CFADs by providing a more detailed spatial context of the average height and coverage of precipitating clouds using a threshold equivalent to the ~15-dB$Z$ Ku minimum sensitivity of the Dual-Frequency Precipitation Radar onboard the GPM *Core Observatory* satellite. The gridded maps were constructed in two steps. First, for each vertical profile from APR-3 within a particular 0.2° longitude × 0.2° latitude box, it was determined whether there were Ku echoes greater than 15 dB$Z$ anywhere within that profile. If maximum reflectivity was greater than 15 dB$Z$, then the highest 15-dB$Z$ bin height was recorded. After all the vertical profiles were processed, the average height of the highest 15-dB$Z$ echo and the percent coverage of vertical profiles containing at least one 15-dB$Z$ echo were calculated for each 0.2° × 0.2° grid box. A one-sample $t$ test was also conducted on the average 15-dB$Z$ echo-top grid boxes to determine where the average 15-dB$Z$ echo-top height significantly differed from the mean echo-top height at a 95% confidence level. Since the individual APR-3 profiles are not independent samples, the average 15-dB$Z$ echo-top height from each flight leg (within a grid box) is used in the significance testing.

### b. *Precipitation data*

#### 1) PRECIPITATION GAUGES

Precipitation rate maps use a combination of OLYMPEX sites (Petersen et al. 2017a) and supplementary sources downloaded from the MesoWest archive (Horel et al. 2002). The OLYMPEX sites used pairs of collocated 20- or 30-cm-diameter tipping buckets except for a high-elevation site that had a single Pluvio$^2$-400 weighing bucket (Petersen et al. 2017b). Similar to Zagrodnik et al. (2018), the average of the two tipping buckets was used if the measurements were within 5% of each other. Otherwise the greater of the two buckets was used since malfunctions tended to reduce the number of tips. The supplementary sources include the Automated Surface Observing System (ASOS), Remote Automated Weather Stations (RAWS), snow telemetry (SNOTEL), and Cooperative Observer Program (COOP). The Hurricane Ridge precipitation measurements are from a heated tipping bucket in a protected location maintained by the Northwest Avalanche Center (NWAC 2018). We carefully monitored and maintained all precipitation measurements in real time throughout OLYMPEX and any sites with missing data during the study period were excluded.

#### 2) DISDROMETERS

Disdrometer measurements (Petersen et al. 2017c) were analyzed at the three sites displayed in Figs. 1a and 2. The Fishery site was located in the near-coastal lowlands approximately 30 km from the coast at an elevation of 52 m. The Prairie Creek site was on the first major windward ridge near Lake Quinault at an elevation of 542 m. The Hurricane Ridge site was within the transition zone between the interior high terrain and lee side at an elevation of 1603 m. The DC-8 flight patterns were configured to fly near or directly above all three sites. Table 1 shows the sample sizes and data-quality statistics during the nine flights used in this study. The precipitation type was determined by the disdrometers. All rain was observed at Fishery and almost all rain at Prairie Creek except for ~15 min of mixed precipitation during three heavier showers on 13 December and a ~2.5-h period of snow on 12 December. Hurricane Ridge recorded all snow during the three prefrontal and three postfrontal flights and all rain during the three warm-sector flights.

Two different types of disdrometers were used in this study. All three sites had second-generation Particle Size and Velocity 2 (PARSIVEL$^2$) disdrometers. The PARSIVEL$^2$ is a laser optical device that measures the size and fall velocity of hydrometeors passing through a 180 mm × 30 mm × 1 mm sheet laser. The raw output contains 32 size and velocity bins from 0.2- to 25-mm diameter with a time resolution of 10 s. The PARSIVEL$^2$ output assumes drops are falling straight down and corrects drops greater than 1 mm for oblateness. The Hurricane Ridge had a Particle Imaging Package (PIP), which is the successor of the Particle Video Imager (Newman et al. 2009). The PIP records high speed (380 frames per second) video of particles passing in front of a halogen lamp located 2 m downwind of the camera. The field of view is 48 mm × 64 mm. The PIP processing software detects and tracks particles as they fall through the observing volume. The software estimates the particle equivalent diameter $D_{eq}$ by drawing a bounding box around the shadowed particle at each frame and fitting an ellipse around the particle within the bounding box. The equivalent diameter is the largest value of the major axis of the

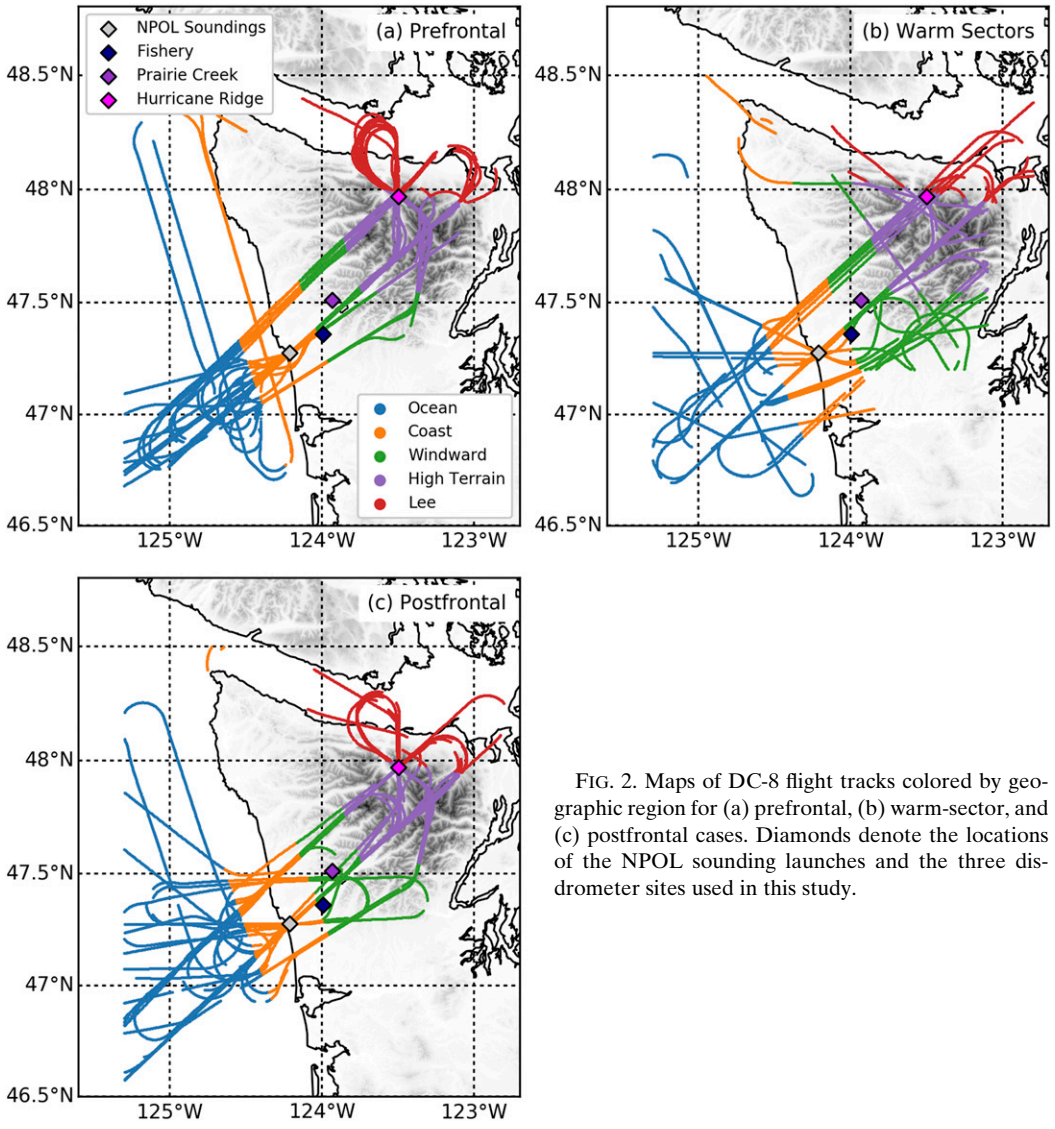


FIG. 2. Maps of DC-8 flight tracks colored by geographic region for (a) prefrontal, (b) warm-sector, and (c) postfrontal cases. Diamonds denote the locations of the NPOL sounding launches and the three disdrometer sites used in this study.

ellipse observed at any time that the particle is in the instrument field of view. The PIP instrument design is further described in Newman et al. (2009) and additional details and nuances of the detection software are found in von Lerber et al. (2017, 2018). The processed output contains 120 size bins from 0.2- to 26-mm diameter with 1-min time resolution. This study uses the PIP measurements at Hurricane Ridge in lieu of the PARSIVEL$^2$ because the PIP operates reliably in strong winds, which occurred frequently at Hurricane Ridge.

### 3) PSDs

Rain and snow particle size distributions (PSDs) are computed and analyzed separately. As in Zagrodnik et al. (2018), the rain PSDs from the PARSIVEL$^2$ were computed following Eq. (6) of Tokay et al. (2014) using terminal fall velocities from Atlas et al. (1973) and excluded periods when the instrument detected frozen precipitation or errors due to condensation/water splashing obstructing the laser optics (Table 1). The PIP rain PSDs came directly from the PIP software, version 1403, described above. This study uses a time interval of 1 min and requires a minimum of at least 50 particles per minute for 1-min samples to be included. Following Thompson et al. (2015) and Zagrodnik et al. (2018) the rain PSDs are described using the median volume diameter $D_o$ and normalized intercept parameter $N_w$ as derived in Testud et al. (2001). This technique is particularly useful because a given PSD with an approximately gamma distribution can be characterized using only $D_o$ and $N_w$. The value of $D_o$ is computed from the binned PSDs by determining the two drop size bins in

TABLE 1. Sample sizes and data-quality statistics from the three disdrometer sites used in this study. At Fishery and Prairie Creek (PARSIVEL$^2$ sites), good data include duration (min) when the disdrometer was functional and reporting rain with no error codes. For Hurricane Ridge (PIP and MRR site), snow is considered good data and the rightmost column additionally constrains the dataset to the duration (min) when the MRR reflectivity at 300 m above the site was $>-10$ dBZ. The MRR was not functioning during the 13 Nov 2015 event.

| | | | Fishery | | Prairie Creek | | Hurricane Ridge | | |
|---|---|---|---|---|---|---|---|---|---|
| Case | Category | Sample size (min) | Good data (%) | >50 particles per minute (%) | Good data (%) | >50 particles per minute (%) | Good data (%) | >50 particles per minute (%) | MRR $>-10$ dBZ (%) |
| 1–2 Dec 2015 | Prefrontal | 239 | 100 | 100 | 100 | 100 | 99 | 81 | 79 |
| 5 Dec 2015 | Prefrontal | 238 | 100 | 100 | 100 | 100 | 100 | 98 | 95 |
| 12 Dec 2015 | Prefrontal | 309 | 100 | 100 | 47 | 47 | 99 | 94 | 85 |
| 13 Nov 2015 | Warm sector | 305 | 75 | 73 | 100 | 100 | 94 | 86 | n/a |
| 3 Dec 2015 | Warm sector | 127 | 100 | 90 | 100 | 92 | 100 | 100 | 100 |
| 8 Dec 2015 | Warm sector | 292 | 100 | 93 | 100 | 100 | 100 | 98 | 98 |
| 4 Dec 2015 | Postfrontal | 201 | 61 | 46 | 71 | 50 | 84 | 71 | 43 |
| 10 Dec 2015 | Postfrontal | 257 | 92 | 63 | 89 | 62 | 100 | 100 | 98 |
| 13 Dec 2015 | Postfrontal | 243 | 82 | 53 | 97 | 89 | 100 | 100 | 89 |

which the cumulative liquid water content reaches 50% and linearly interpolating between those two bins (Hardin and Guy 2017). The value of $N_w$ is computed using $D_o$ in Eq. (8) of Testud et al. (2001).

The irregular shape of ice particles makes PSD parameterization more difficult for snow than rain. This study considers histograms of 1-min values of $D_o$, particle concentration, and maximum diameter $D_{\max}$. The value of $D_{\max}$ is approximated by the midpoint of the largest bin with at least one particle. Although the PIP was located on the roof of a ~2.5-m-tall building, the PSDs at Hurricane Ridge could still be contaminated at times by blowing snow or snow falling and blowing from nearby trees. To mitigate this problem, 1-min PSDs are only retained if the collocated K-band (24 GHz) Micro Rain Radar (MRR) measured reflectivity of $>-10$ dB$Z$ at 300 m above the disdrometer. Table 1 shows that the MRR most significantly reduced the sample on 4 December owing to weak shallow echo, which could have been due to tiny snowflakes, blowing snow, or a combination of both.

### c. *Soundings*

A Colorado State University sounding unit at NASA's S-band polarimetric radar (NPOL) site on the Pacific Coast (Fig. 1) obtained rawinsonde soundings during all DC-8 flights. These data from these measurements were quality controlled following Ciesielski et al. (2014). At least one sounding was launched during each DC-8 flight, which averaged 4.1 h of observing time. If multiple soundings were launched during a flight, the sounding nearest the middle of the flight was used for analysis. Vertical profiles of moist static stability $N_m^2$ (Durran and Klemp 1982) were created by linearly interpolating sounding data to 200-m height intervals and computing $N_m^2$ over each layer.

## 3. Synoptic overview and case selection

Maritime frontal systems have distinct cloud and precipitation features within different sectors bounded by the warm, cold, and/or occluded fronts (Nagle and Serebreny 1962; Houze et al. 1976; Matejka et al. 1980; Houze and Hobbs 1982; Medina et al. 2007; Houze et al. 2017; Zagrodnik et al. 2018). The prefrontal (or early) sector is associated with the initial period of stratiform precipitation as the warm or occluded front approaches the coast. Warm sectors are located to the south of the surface low pressure center between the warm front and cold-frontal zone. Postfrontal sectors are located behind the cold or occluded front in a region of cold advection over the relatively warm waters of the Pacific Ocean. As described below, storm sectors were classified using

soundings. The classifications are consistent with PK18, with the caveat that prefrontal periods in this study can refer to the period prior to a warm or occluded front. PK18 excluded occluded fronts including 1–2 and 12 December.

Nine OLYMPEX APR-3 flights produced 37.1 measurement hours, which we have divided into three categories based on the storm sector in which they occurred. Eight flights were excluded because of instrumentation problems, limited sampling due to short mission length, isolated/nonexistent precipitation, or a flight pattern not over the Olympic Mountains. Figure 2 shows the flight tracks divided by storm sector. Colors denote five geographic regions used to subdivide the data for CFADs: ocean, coast, windward, high terrain, and lee. The DC-8 flew a remarkably consistent southwest–northeast-oriented ovular "racetrack" pattern covering all five regions, with occasional deviations.

Table 2 contains the breakdown of APR-3 observation time by geographic region for each case. An APR-3 profile is defined as a single nadir profile. The 3 December flight had the shortest flight duration and least number of profiles. The 13 November flight had a small number of profiles relative to the flight duration because some of the legs extended outside of the study domain. Eight of the nine missions sampled all five of the geographic regions, except there were no leeside measurements on 13 November. The ocean was the most sampled of the five regions, accounting for 29% of the included profiles. The lee side received the least sampling, 10% of the total. The coast, windward, and high-terrain regions each accounted for about one-fifth of the total profiles.

The variability among storm sectors is readily apparent in the infrared satellite images and overlaid 500-hPa contours shown in Fig. 3 from each of the nine flights used in this study. The three subsections below describe the synoptic conditions that were used to classify the flights into prefrontal (Figs. 3a–c), warm sector (Figs. 3d–f), and postfrontal (Figs. 3g–i) sectors.

### *a. Prefrontal*

The three prefrontal cases in Figs. 3a–c each contained a broad shield of −40°C or colder cloud tops covering western Washington State and the near-coastal waters with embedded colder cloud tops likely associated with mesoscale elements (Houze et al. 1976; Hobbs 1978; Matejka et al. 1980). The sounding-derived parameters for each case in Table 3 show that the prefrontal sectors all had low-level flow veering from southeasterly at 925 hPa to southwesterly at 700 hPa and high static stability in the 950–850-hPa layer, a consequence of warm advection associated with the

TABLE 2. Characteristics of each of the nine cases in this study, including storm sector, flight times, the number of APR-3 vertical profiles, and the percentage of profiles observed in each geographic sector. The percentage values are computed with respect to the full sample in each geographic sector so that the columns add up to 100%.

| Case | Category | APR-3 start time (UTC) | APR-3 end time (UTC) | No. of APR-3 profiles | Ocean (%) | Coast (%) | Windward (%) | High terrain (%) | Lee (%) |
|---|---|---|---|---|---|---|---|---|---|
| 1–2 Dec 2015 | Prefrontal | 2126 | 0124 | 7426 | 13.6 | 12.2 | 10.6 | 15.8 | 12.3 |
| 5 Dec 2015 | Prefrontal | 1421 | 1818 | 6873 | 8.6 | 10.8 | 13.4 | 13.8 | 19.0 |
| 12 Dec 2015 | Prefrontal | 1611 | 2119 | 7653 | 13.1 | 16.3 | 11.2 | 11.2 | 17.2 |
| 13 Nov 2015 | Warm sector | 1417 | 1921 | 5179 | 12.3 | 10.3 | 12.7 | 4.6 | 0.0 |
| 3 Dec 2015 | Warm sector | 1443 | 1649 | 3027 | 2.9 | 5.6 | 6.0 | 7.4 | 6.2 |
| 8 Dec 2015 | Warm sector | 1333 | 1824 | 6356 | 10.9 | 9.7 | 12.0 | 12.0 | 11.9 |
| 4 Dec 2015 | Postfrontal | 1330 | 1650 | 6471 | 12.3 | 12.7 | 12.1 | 9.9 | 7.7 |
| 10 Dec 2015 | Postfrontal | 1513 | 1929 | 7017 | 15.3 | 11.5 | 10.7 | 11.7 | 9.9 |
| 13 Dec 2015 | Postfrontal | 1413 | 1815 | 6845 | 10.9 | 10.8 | 11.2 | 13.7 | 15.9 |

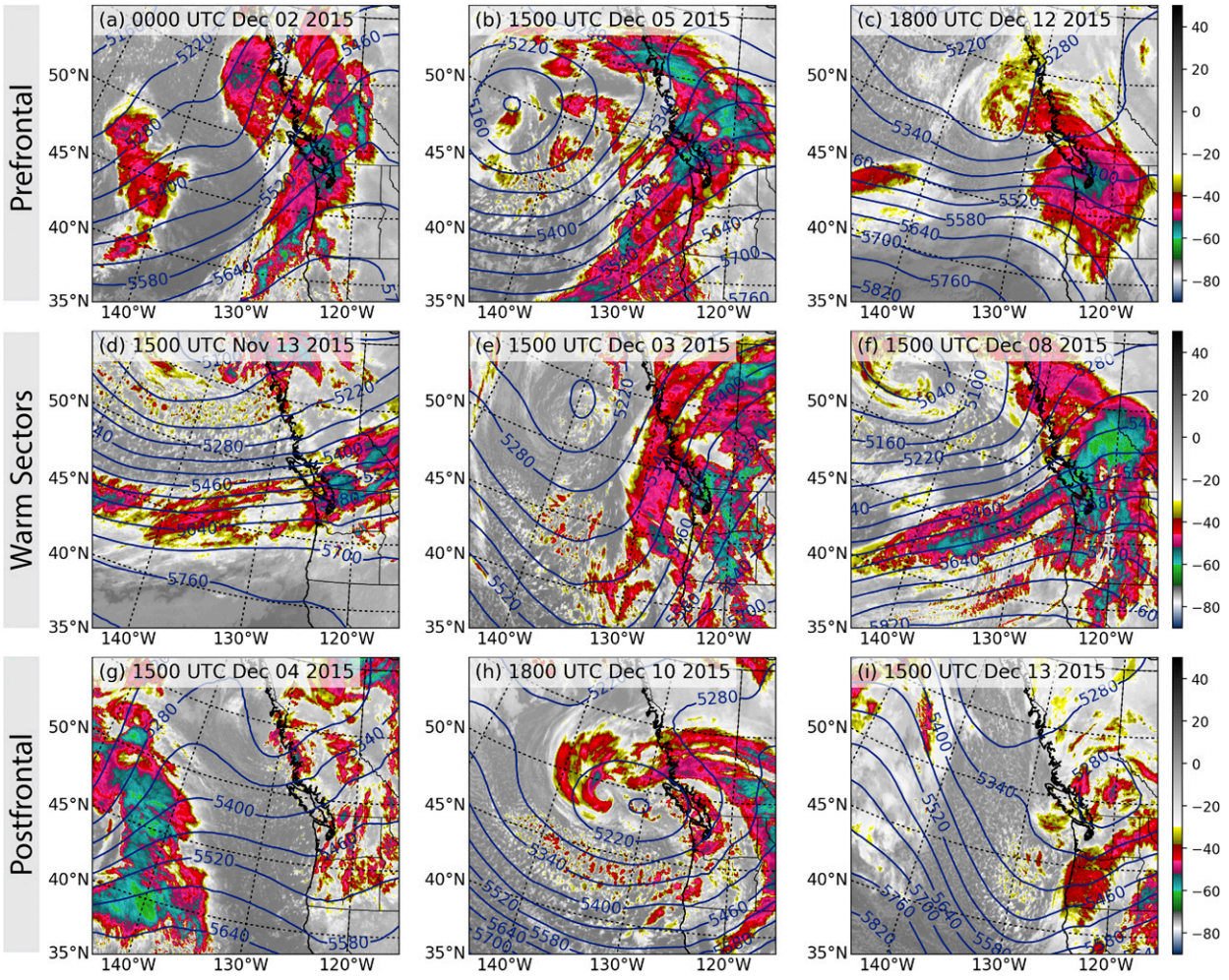


FIG. 3. GOES-West infrared imagery (filled contours; °C) and North American Regional Reanalysis (NARR) 500-hPa heights (blue contours; m) for the closest NARR analysis time for the nine cases listed in Table 2: (a) 0000 UTC 2 Dec, (b) 1500 UTC 5 Dec, (c) 1800 UTC 12 Dec, (d) 1500 UTC 13 Nov, (e) 1500 UTC 3 Dec, (f) 1500 UTC 8 Dec, (g) 1500 UTC 4 Dec, (h) 1800 UTC 10 Dec, and (i) 1500 UTC 13 Dec 2015.

approaching warm or occluded front. The hodographs in Fig. 4 and the moist static stability profiles in Fig. 5 both confirm stable stratification during these three prefrontal periods and veering low-level flow in the 1–3-km layer, conditions that were conducive to blocked or deflected low-level flow. High values of integrated vapor transport (IVT; 500–600 $\mathrm{kg\,m^{-1}\,s^{-1}}$) and 20–30 $\mathrm{m\,s^{-1}}$ flow at 925 hPa (Table 3) indicate strong synoptic-scale forcing. The greatest variability between cases is seen in the melting-level height, as the lower 500-hPa heights and more westerly flow aloft (Fig. 3c) suggested a much lower 0°C isotherm on 12 December than in the other two prefrontal cases.

### b. *Warm sectors*

The warm-sector IR satellite images (Figs. 3d–f) show a nonuniform, broken pattern of colder cloud tops in the vicinity of the Olympic Peninsula with approaching banded clouds to the west or northwest associated with the cold frontal band. Although the soundings always resembled warm-sector conditions, some precipitation associated with the approaching frontal band was sampled in this study. Consistent with the alignment of the 500-hPa geopotential height contours, the 925-hPa wind directions in Table 3 show that the low-level (925 hPa) flow impinged on the southern side of the Olympic Peninsula on 3 December and the west-southwest side on 13 November and 8 December. The hodographs (Fig. 4b) show less veering than the prefrontal sector and the moist static stability profiles (Fig. 5) were fairly close to moist neutral at low levels, especially from 1 to 4 km. The combination of high melting level (2–3 km), strong IVT (>500 $\mathrm{kg\,m^{-1}\,s^{-1}}$; Table 3), and moist-neutral stability

TABLE 3. Synoptic parameters derived from soundings launched at the NPOL radar site shown in Fig. 1a for each case.

| Case | Category | NPOL sounding (UTC) | IVT ($kg\,m^{-1}\,s^{-1}$) | Melting level (m) | 925-hPa wind speed ($m\,s^{-1}$) | 925-hPa wind direction (°) | 700-hPa wind speed ($m\,s^{-1}$) | 700-hPa wind direction (°) | 950–850-hPa $N_m^2$ ($\times 10^{-4}$) |
|---|---|---|---|---|---|---|---|---|---|
| 1–2 Dec 2015 | Prefrontal | 2317 | 500 | 2103 | 23.3 | 166 | 17.6 | 218 | 1.06 |
| 5 Dec 2015 | Prefrontal | 1514 | 560 | 2031 | 30.3 | 160 | 18.3 | 216 | 0.98 |
| 12 Dec 2015 | Prefrontal | 1914 | 529 | 879 | 21.1 | 158 | 28.1 | 234 | 1.31 |
| 13 Nov 2015 | Warm sector | 1632 | 575 | 2583 | 22.0 | 240 | 19.0 | 250 | 0.19 |
| 3 Dec 2015 | Warm sector | 1516 | 784 | 2150 | 26.2 | 172 | 33.3 | 203 | −0.21 |
| 8 Dec 2015 | Warm sector | 1515 | 815 | 2769 | 52.2 | 214 | 32.3 | 231 | 0.64 |
| 4 Dec 2015 | Postfrontal | 1517 | 99 | 1219 | 8.8 | 235 | 11.5 | 256 | −0.68 |
| 10 Dec 2015 | Postfrontal | 1736 | 393 | 1344 | 24.8 | 233 | 23.1 | 233 | −0.82 |
| 13 Dec 2015 | Postfrontal | 1516 | 187 | 1027 | 15.1 | 289 | 17.0 | 265 | −0.47 |

suggest that all these of these warm sectors contained corridors of strong horizontal vapor transport commonly referred to as atmospheric rivers (e.g., Ralph et al. 2004).

### c. *Postfrontal*

The postfrontal IR satellite images (Figs. 3g–i) all show regions of open-cellular convective elements with embedded mesoscale features located along and offshore of the Washington coast. There is considerable case-to-case variability in the amplitude and position of the upper-level trough. Variability in the large-scale synoptic environment is reflected by differences in low-level wind amplitude and direction (Fig. 4c; Table 3). However, the moist static stability (Fig. 5) profiles were nearly identical: unstable below 1.5 km and close to moist neutral above 1.5 km. Other commonalities include relatively low melting levels (1–1.4 km; Table 3), weak IVT ($<400\,kg\,m^{-1}\,s^{-1}$; Table 3), and weak directional wind shear (Fig. 4c).

## 4. Results

### a. *Prefrontal*

#### 1) REFLECTIVITY STRUCTURE

To illustrate examples of some of the features noted below in the statistical distributions, Fig. 6 shows transects of APR-3 Ku-band reflectivity across the full Olympic Mountains range, one from each storm sector. The prefrontal example (Fig. 6a) shows stratiform precipitation upstream of the mountains with relatively uniform echo height. The echo tops sloped downward from the windward side to the high terrain and there was a complete loss of reflectivity over the lee side. The near-surface reflectivity eventually recovered farther downstream to the northeast of the Olympic Mountains (Fig. 6b).

All of the APR-3 transects from the three prefrontal periods (as described in section 2a) are aggregated into normalized Ku-band reflectivity CFADs in Fig. 7 for the full sample (Fig. 7a) and for the five geographic regions shown in Fig. 2 (Figs. 7b–e). In general, the mode of reflectivity decreases at a constant slope with height from 20–30 dB$Z$ at 1 km to ≤10 dB$Z$ above 6 km. The outlier contours (10%, 30%) are fairly close to the modal contours (50%, 70%, 90%), suggesting a narrow distribution that lacks temporal variability. Both of these characteristics indicate a predominance of a uniform, mature stratiform echo. The one CFAD that deviates from this pattern is the lee side, which had substantially

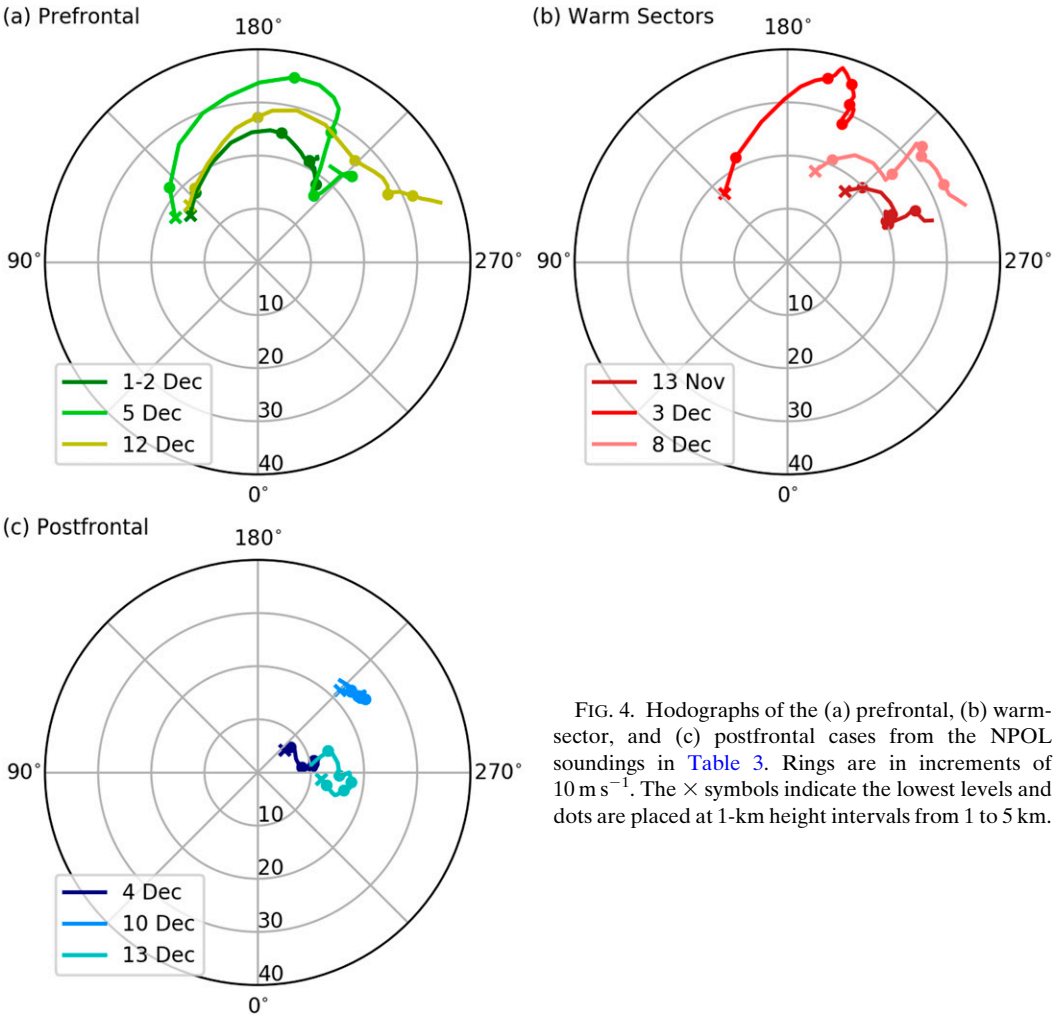


FIG. 4. Hodographs of the (a) prefrontal, (b) warm-sector, and (c) postfrontal cases from the NPOL soundings in Table 3. Rings are in increments of 10 m s$^{-1}$. The × symbols indicate the lowest levels and dots are placed at 1-km height intervals from 1 to 5 km.

lower reflectivity below 3 km despite appearing similar to the other regions above 3 km.

Differences in reflectivity between regions are highlighted in Fig. 8, where the coast, windward, high-terrain, and lee-normalized CFADs are subtracted from the normalized ocean CFAD. In general, laterally adjacent positive (red) and negative (blue) contours indicates intensification or weakening of reflectivity at a particular height level. An area of positive or negative contours without a corresponding region of the opposite sign indicates a change in the shape of the distribution as a whole, either a narrowing–broadening or a shift in the mode to a different height level. In Fig. 8b, the rightward shift to a higher frequency of reflectivities greater than 20 dB$Z$ and lower frequency of reflectivities below 20 dB$Z$ at levels between 2.5 and 5.0 km indicates modest enhancement of reflectivity over the windward slopes. The high-terrain pattern (Figs. 7e, 8c) is caused by a narrow increase in ~25-dB$Z$ reflectivity below 3 km. Leeside reflectivities (Figs. 7f, 8d) in the 20–30-dB$Z$ range are diminished most prominently in the lower levels. Overall, these patterns indicate modest enhancement predominately upstream of high terrain and rapid diminishment at lower levels on the lee side.

Figure 9 supplements the CFADs by showing the geographic distribution of the average height of the 15-dB$Z$ echo top and the coverage of profiles containing at least 15-dB$Z$ reflectivity at any height in locations with sufficient aircraft coverage. Prefrontal cases experience a very slight increase in 15-dB$Z$ echo tops over the windward slopes on the south side of the Olympic Mountains (Fig. 9a). Incoming flow may be lifting over the stably stratified lower layer (Fig. 5), leading to higher echo tops upstream of terrain, similar to results shown upstream of other mountain ranges by Houze et al. (2001) and James and Houze (2005). The discontinuity in the bright band along the windward

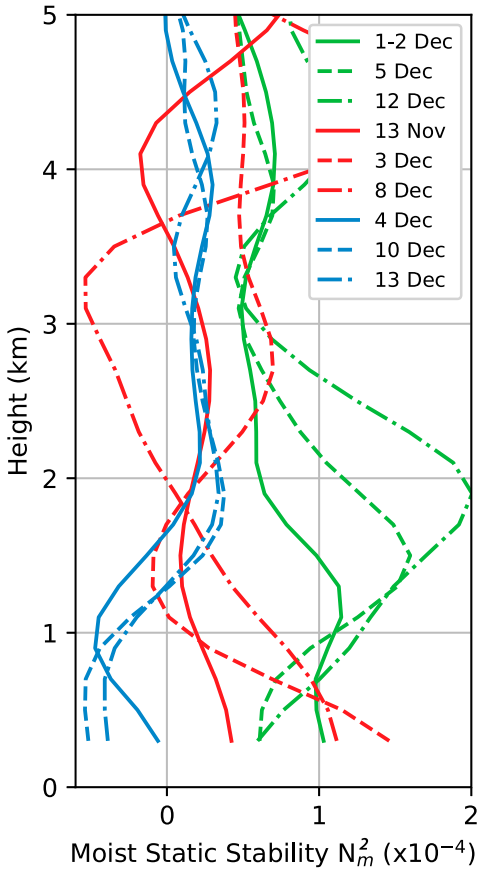


FIG. 5. Vertical profiles of moist static stability $N_m^2$ ($\times 10^{-4}\,s^{-2}$) derived from the NPOL soundings for each of the nine cases detailed in Table 3. The green profiles are for the prefrontal cases, red for the warm-sector cases, and blue for the postfrontal cases.

slopes in Fig. 6a could also be indicating upstream lifting or possibly blocked cold air in the Quinault Valley (Colle 2004; Smith and Barstad 2004; Minder et al. 2011). PK18 showed that terrain-induced gravity waves tilted upstream with height (Durran 1990) contributed to the apparent upstream enhancement. Echo coverage of greater than 15 dB$Z$ was nearly 100% everywhere during the prefrontal flights, except for a sharp decline to less than 25% coverage on the northeast side of the Olympic Mountains (Fig. 9b).

### 2) PRECIPITATION CHARACTERISTICS

Figure 10 shows histograms of 1-min $D_o$ and $\log(N_w)$ derived from rain PSDs measured by PARSIVEL$^2$ disdrometers at the Fishery site (solid lines) and Prairie Creek site (dashed lines). Each case is shown as a separate line. The rain PSDs at the Fishery and Prairie Creek are tightly clustered between $1 < D_o < 1.5$ mm and $3 < \log(N_w) < 4\,m^3\,mm^{-1}$ (Figs. 10a,b). This range is consistent with the "most frequent" PSD regime defined in Zagrodnik et al. (2018) which was associated with synoptic conditions resembling the prefrontal sector, specifically stable stratification at low levels and southeasterly 925-hPa winds that do not impinge directly on the southwesterly facing terrain. The distributions of $D_o$ and $N_w$ show little variability between cases or sites, consistent with the nearly identical average precipitation rates at the two sites (3.4 mm h$^{-1}$ at Fishery; 3.3 mm h$^{-1}$ at Prairie Creek) during the prefrontal cases. Prairie Creek did favor slightly larger drops than Fishery, possibly a by-product of the slight enhancement above the melting level on the windward side seen in Fig. 8b. In general, the prefrontal PSDs represent characteristic stratiform precipitation dominated by drops of modest size and concentration.

The snow particle size and number histograms at Hurricane Ridge are shown in Fig. 11. The prefrontal snow PSDs (Fig. 11, left column) show a surprising amount of case-to-case variability given the relatively uniform rain PSDs on the windward side. Large concentrations of small particles dominated on 12 December and almost no particles larger than 6–7-mm diameter were observed (Figs. 11c,e). The other two prefrontal cases had a greater variety of particle sizes and concentrations including a longer $D_{max}$ tail reaching values of 10–15 mm. Two possible causes of higher particle concentrations on 12 December are colder temperatures at Hurricane Ridge (Fig. 11a) and stronger cross-barrier winds at 700 hPa (Table 3), both of which may lead to turbulent motions that are unfavorable for observing snow aggregates at the surface (Houze 2014). The stronger cross-barrier winds on 12 December may have also advected more particles over from the windward side, as the 15-dB$Z$ echo-top heights had less decline from windward side to the high terrain compared to the other two prefrontal cases (not pictured). As a whole, these three cases suggest that high-terrain snow PSDs tend to be more variable than rain PSDs in prefrontal sectors, although the CFADs in Fig. 7 indicate that there are no inherent differences in reflectivity structure over the high terrain compared with the coast and windward side.

As a way to summarize the characteristics of the precipitation structure in each storm sector, Fig. 12 provides the average hourly precipitation rate during APR-3 flights at the various ground sites for the different storm sector cases. The corresponding rain rates at the disdrometer sites for each case are presented in Table 4. For the prefrontal cases, the average prefrontal precipitation rates were highest (~3–5 mm h$^{-1}$) on the coast and the southern side of the Olympic Mountains (Fig. 12a). On the southwest side of the mountains there was minimal difference in precipitation

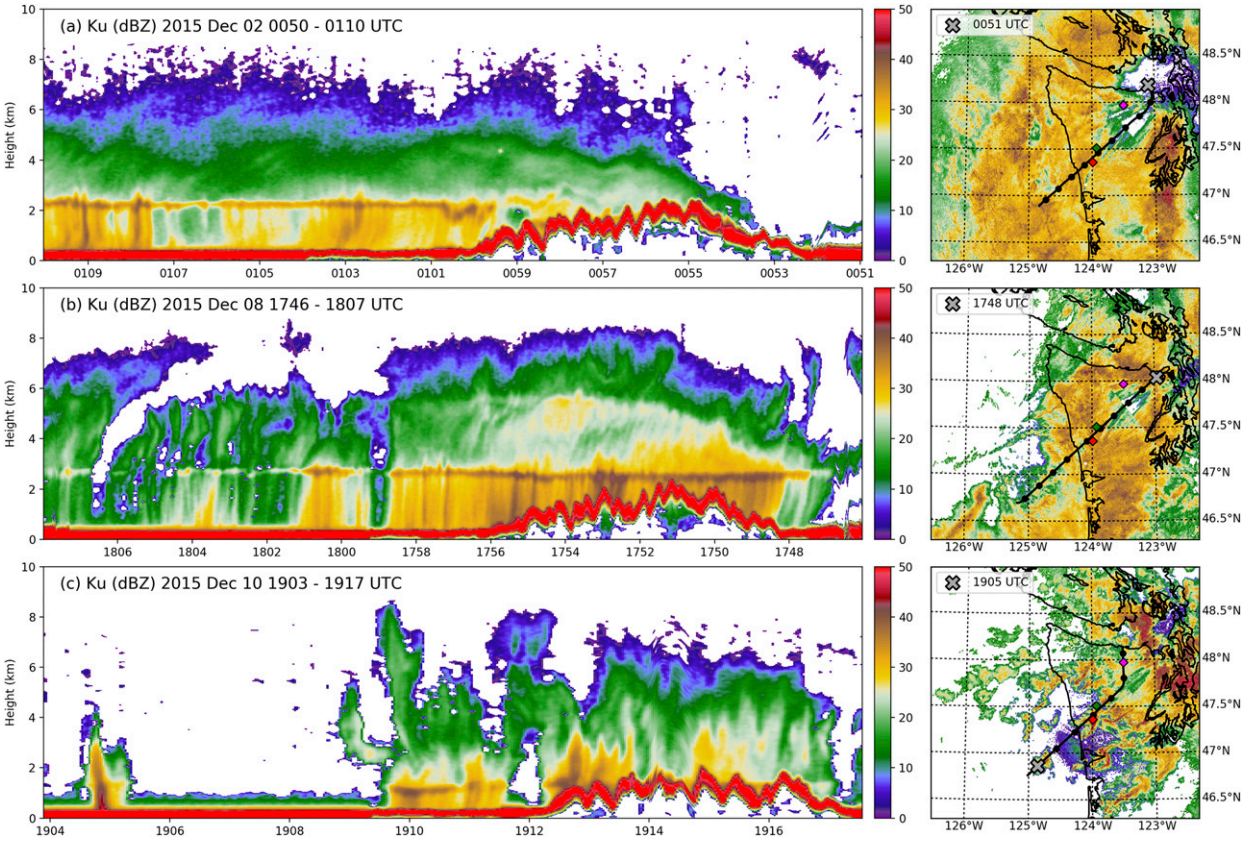


FIG. 6. (left) Time–height cross sections of APR-3 Ku reflectivity and (right) flight-track maps for (a) 2, (b) 8, and (c) 10 Dec 2015. Composited PPI scans of reflectivity at 0.5° azimuth from the Langley Hill (KLGX) and Whidbey Island (KATX) radars are included in the right column. The times in the left column match the black dots in the right column with the × denoting the starting time of the cross section. Colored diamonds denote the disdrometer site locations as in Fig. 1.

rate between the coast and the Quinault Valley and neighboring windward slopes, consistent with the lack of appreciable enhancement in the CFADs (Fig. 8). Precipitation rates fell off rapidly to 1 mm $h^{-1}$ or less across the high terrain and lee side.

### *b. Warm sectors*

#### 1) REFLECTIVITY STRUCTURE

The APR-3 transect in Figs. 6c and 6d nicely illustrates some of the key differences between prefrontal and warm-sector reflectivity structures. This example clearly shows deep echo over the windward and high-terrain regions with a secondary enhancement layer around 5 km. The echo extended to the lee side in spite of the reduction in height of the echo top. The echo on the lee side was especially pronounced within and above the bright band (3–4 km), suggesting downstream advection of ice particles that were formed over the terrain. Reduction of echo was much less than was found for the prefrontal cases (Fig. 6a). The near-surface reflectivity in Fig. 6d confirms the reduced rain shadow relative to the prefrontal example in Fig. 6b.

The normalized warm-sector CFADs in Fig. 13 differ markedly from the prefrontal CFADs in Fig. 7. All of the CFADs have broader distributions then the prefrontal CFADs at any given height, suggesting a greater variety of sizes and/or concentrations of hydrometeors. Rather than a constant slope with height, both the overall modal and outlier contours (Fig. 13a) have two rightward bulges associated with larger reflectivity: one between 2 and 3 km associated with the bright band and the other between 4 and 6 km associated with a secondary enhancement layer aloft. A secondary enhancement in the ice layer was previously observed over coastal terrain in California by Kingsmill et al. (2006), in the Oregon Cascades by Medina et al. (2007), and in OLYMPEX by McMurdie et al. (2018). Collocated APR-3 and in situ Citation aircraft observations in the 3 December 2015 case (Chase et al. 2018) showed spherical ice particles and rimed aggregates within a region of enhanced reflectivity at 4-km elevation.

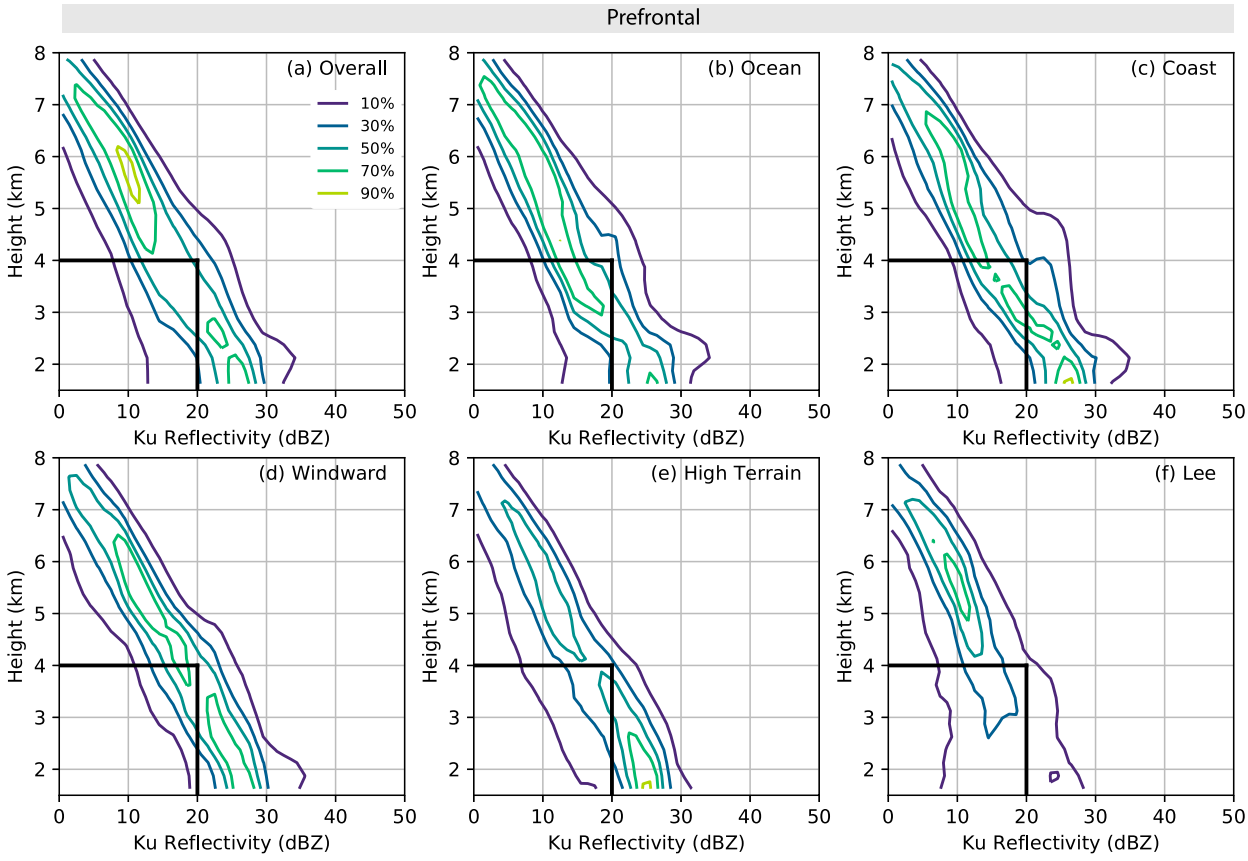


FIG. 7. Prefrontal CFADs of APR-3 Ku-band reflectivity for (a) all geographic regions and (b)–(f) the five geographic regions denoted in Fig. 2. The CFADs are normalized where each frequency is divided by the maximum overall frequency, and contours represent the frequency of occurrence relative to the maximum absolute frequency. Thick black lines at 4 km and 20 dB$Z$ are for reference. Heights are relative to sea level.

Figure 14 shows that this secondary enhancement is most pronounced over the windward slopes and high terrain above the bright band in the 3–6-km layer.

Another noteworthy feature in the warm-sector normalized CFADs is the relatively low height of the modal contours, especially over land (Figs. 13c,d,e,f). The increased frequency of lower-level reflectivities without accompanying increases at upper levels suggests the importance of low-level enhancement processes over terrain. The low-level mode in reflectivity (>50% contours below 2 km) tends to be relatively weak over the ocean (mode of 10–25 dB$Z$) but increases slightly at the coast and especially over terrain. In the windward and high-terrain regions (Figs. 14b,c) the enhancement signature is present throughout the precipitating cloud, suggesting a juxtaposition of enhancement in both the ice and liquid portions of the precipitating cloud. The varying role of these precipitation-generating processes was explored in Zagrodnik et al. (2018) and is further described with disdrometer observations in the next section.

Unlike the prefrontal sector, the warm-sector enhancement signature reaches farther downstream to the lee side (Figs. 13f, 14d), where more frequent occurrence of stronger reflectivities relative to the ocean are seen more prominently below 3 km. The progressive lowering of the ice enhancement layer from the windward to high-terrain to lee regions in Figs. 14b, 14c, and 14d indicates the advection of ice particles by strong cross-barrier winds (Table 3; Fig. 4) originating from the deeper layer of clouds over the windward and high-terrain regions. Two of the three warm-sector cases had 700-hPa winds in excess of 30 m s$^{-1}$ (Table 3). It is possible that enhanced microphysical growth within the secondary enhancement in the ice layer at 4–6 km previously discussed could be contributing to the increased downstream spillover in warm sectors, a postulation supported by the brightband enhancement signature at 2–2.5 km in Fig. 14d. Spillover may also be fostered by reduced leeside descent in warm sectors (PK18).

Maps of 15-dB$Z$ height and coverage corroborate the precipitation processes described above (Figs. 9c,d).

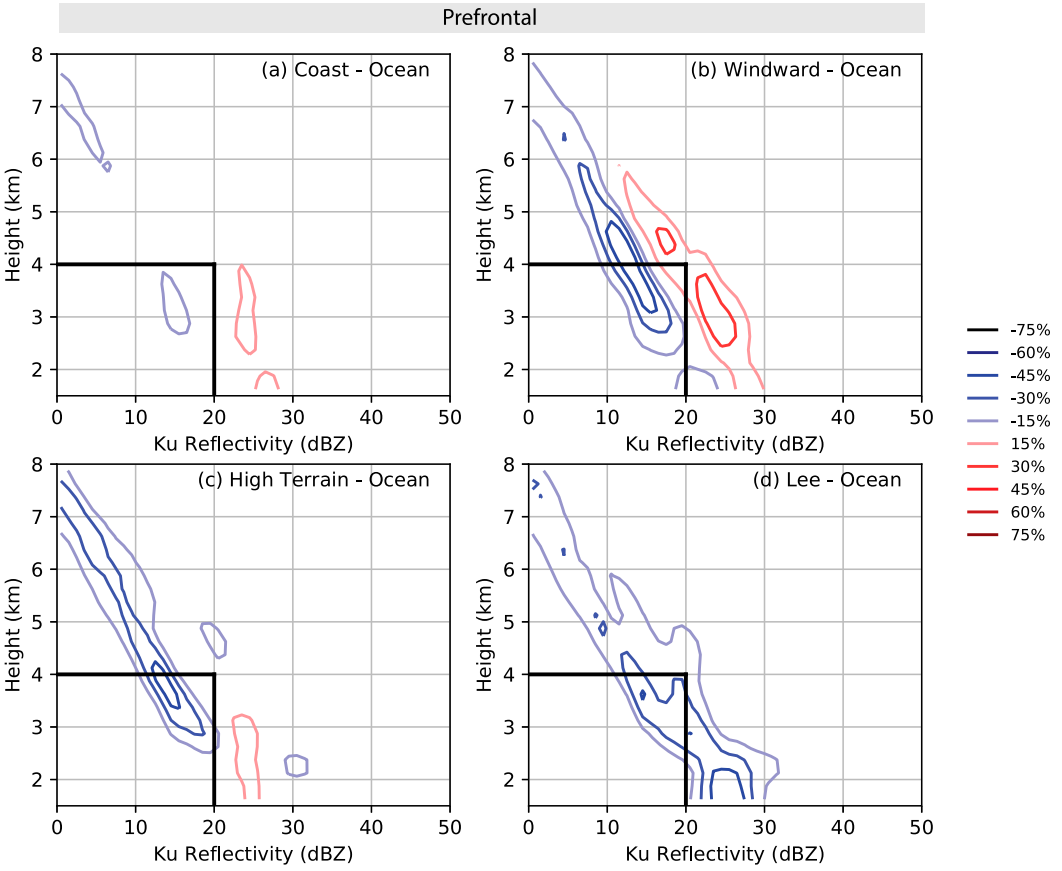


FIG. 8. Prefrontal difference CFADs computed by subtracting the ocean CFAD in Fig. 7b from the (a) coast, (b) windward, (c) high-terrain, and (d) leeside CFADs. Contours represent the frequency difference between the two geographic regions. Thick lines at 4 km and 20 dB$Z$ are for reference.

Precipitating clouds have relatively low average height and only about 50% spatial coverage over the ocean and coast in the warm sectors. The maximum height and coverage of 15-dB$Z$ echo was over 5.5 km and located directly over the Olympic Mountains range. In warm sectors, complex terrain is responsible for both the enhancement of preexisting precipitation as well as the generation of additional and/or stronger precipitating clouds to reach 100% coverage. The precipitating cloud decreases in height downstream of the highest terrain, but precipitation is advected to the lee side, resulting in 80%–100% coverage of >15-dB$Z$ echo over most of the northeast side of the Olympic Peninsula (Fig. 9b).

### 2) PRECIPITATION CHARACTERISTICS

Compared to the prefrontal sector, the warm-sector rain-parameter histograms in Figs. 10c and 10d have broader distributions within individual cases, greater case-to-case variability, and more significant differences between the Fishery and Prairie Creek sites. The 3 December case bears the closest resemblance to the prefrontal histograms with relatively similar distributions at Fishery and Prairie Creek peaking at similar $D_o$ and $N_w$ values. In contrast, 13 November and 8 December have broad distributions of $D_o$ and $N_w$ with greater differences between Fishery and Prairie Creek. Table 4 shows that these two cases also featured considerably higher rain rates at Prairie Creek (14 mm h$^{-1}$) than Fishery (5 mm h$^{-1}$) while on 3 December the rain rate at Prairie Creek was nearly identical to Fishery (~3 mm h$^{-1}$ at both sites). The main synoptic difference was the southerly direction of the low-level winds on 3 December (Table 3; Fig. 4b), which does not favor enhancement of precipitation on the southwest (Quinault) side of the Olympic Mountains where the ground sites were located. Previous studies show that the direction of the low-level flow and IVT vector strongly influences the location of heavy precipitation within atmospheric river events (Neiman et al. 2011; Hecht and Cordeira 2017), by favoring warm precipitation processes over the low- to midelevation

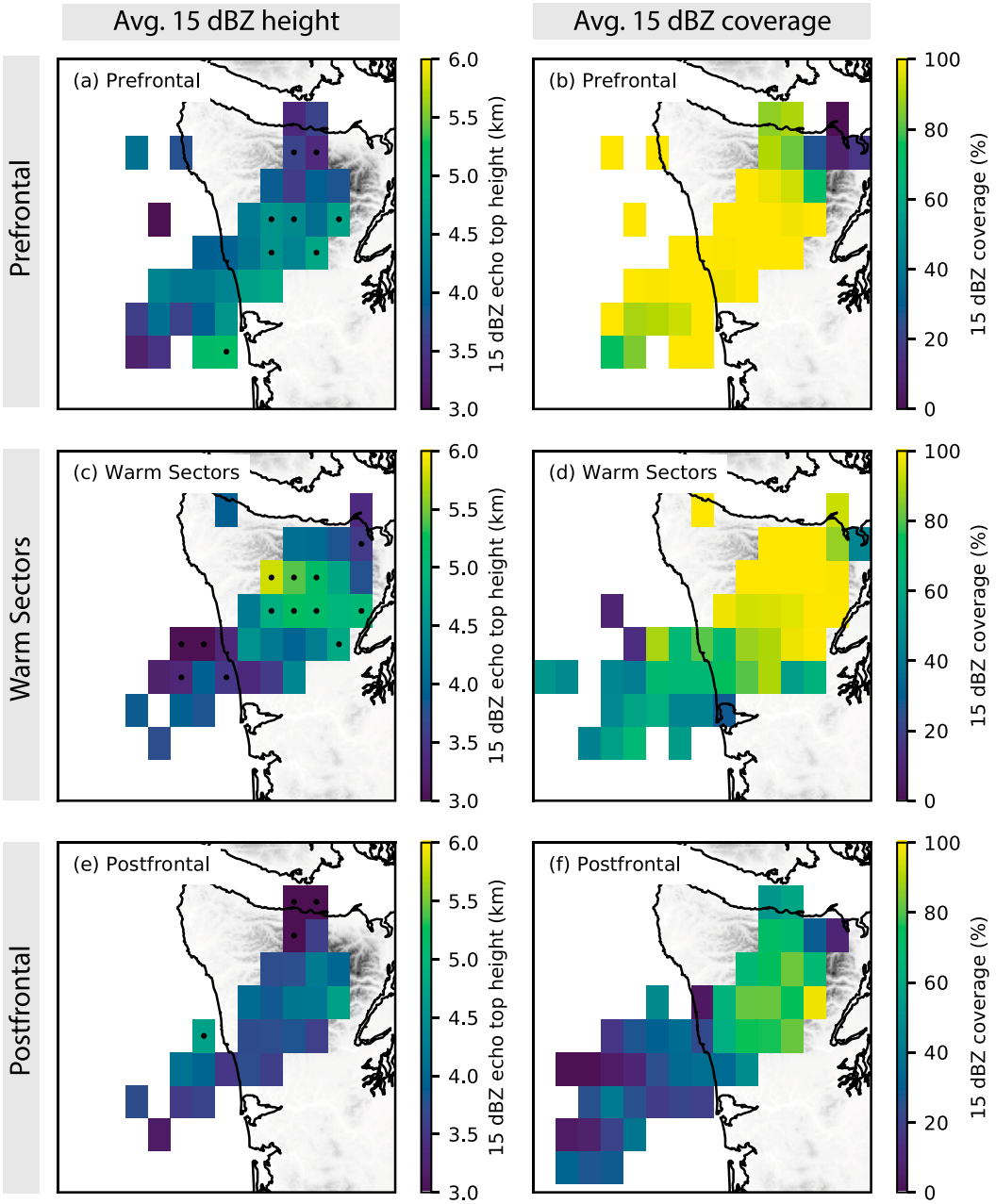


FIG. 9. Gridded maps (0.2° × 0.2°) of APR-3 Ku-band average (left) 15-dB$Z$ echo-top height (km) and (right) frequency of >15-dB$Z$ reflectivity at any height level (%) for (a),(b) prefrontal, (c),(d) warm-sector, and (e),(f) postfrontal cases. The dots in the left column represent grid boxes with statistically different means than the average (using a one-sample $t$ test, at the 95% confidence interval).

windward slopes that are directly impinged on by the low-level flow (Zagrodnik et al. 2018).

Figure 15 shows the warm-sector rain $D_o$ and $N_w$ distributions over the high terrain at Hurricane Ridge. Figures 10 and 15 should not be quantitatively compared because the PIP and PARSIVEL$^2$ have different sensitivities to small particles. The relative shapes of the distributions at Hurricane Ridge are narrower than Fishery and Prairie Creek. Also, the 3 December case is not much of an outlier. Instead, all of the distributions closely resemble the prefrontal rain PSDs on the windward side (Figs. 10a,b). In a three-dimensional (dome shaped) mountain range like the Olympic Mountains, the low-level flow orientation appears to have a lesser

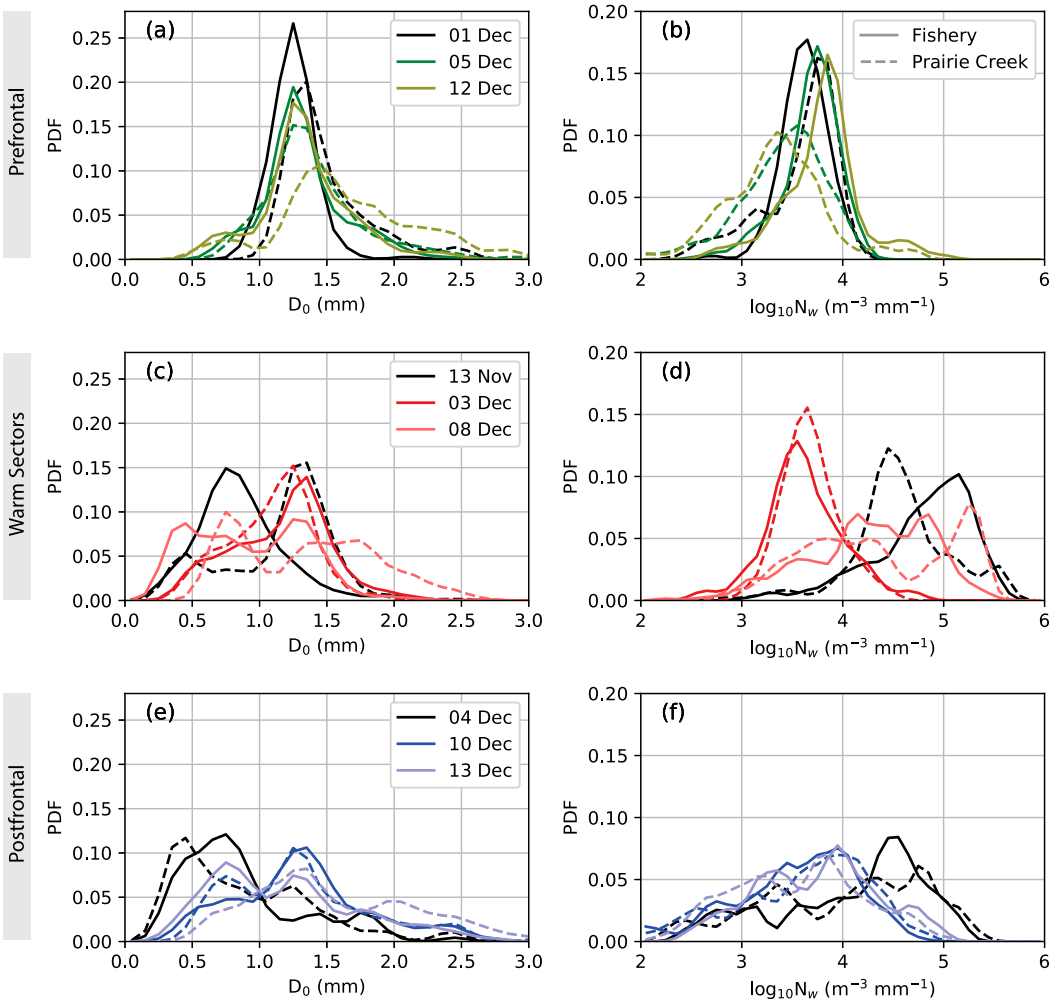


FIG. 10. Histograms of 1-min (left) $D_o$ and (right) $N_w$ measured by PARSIVEL$^2$ disdrometers at Fishery (solid lines) and Prairie Creek (dashed lines) for (a),(b) prefrontal, (c),(d) warm-sector, and (e),(f) postfrontal cases.

influence over the high terrain than the windward slopes, thus reducing the difference in PSD between 3 and 8 December at Hurricane Ridge. Presumably most of the high-terrain precipitation originated from ice processes above the bright band. The Hurricane Ridge PSDs may also be reflecting microphysical changes occurring within the spillover process. Two possibilities are particle segregation as larger particles preferentially fall out upwind of Hurricane Ridge and particle breakup as a consequence of the strong cross-barrier flow (Table 3).

The map of average warm-sector precipitation rates (Fig. 12b) shows a sharp increase in precipitation rates from 1 to 2 mm h$^{-1}$ at the coast to a maximum of 8–11 mm h$^{-1}$ (Fig. 12b) on the low- to midelevation windward slopes. These low rain rates at the coast imply that the overwhelming majority of warm-sector precipitation occurs as a consequence of flow modification by the Olympic Mountains (Zagrodnik et al. 2018). The variety of PSDs associated with windward-side precipitation implies that, consistent with the CFADs (Figs. 13, 14), orographically enhanced precipitation may originate from particles generated in the ice layer, liquid layer, or a combination of both.

Modest precipitation rates of 0.4–2.4 mm h$^{-1}$ were observed on the lee side. While these precipitation rates are objectively unimpressive, they may contribute an appreciable fraction of the modest seasonal precipitation totals in the drier lee side. Given the presumed advection and fallout time scales of ice particles and the progressively lower height of the upper-level enhancement over the windward, high terrain, and lee side (Figs. 14b–d), ice particles produced within the secondary enhancement layer are likely falling out farther

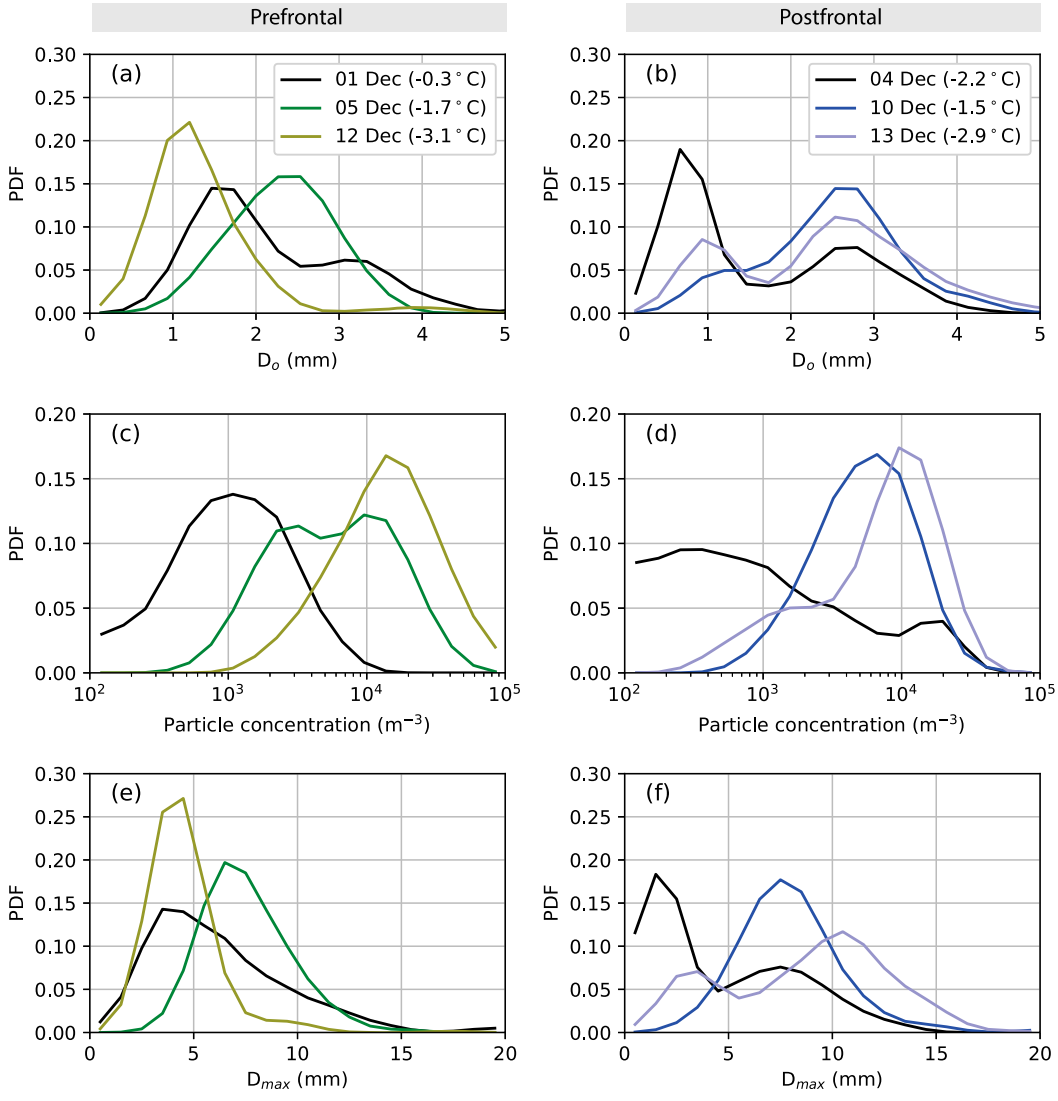


FIG. 11. Histograms of 1-min (a),(b) $D_o$, (c),(d) particle concentration, and (e),(f) $D_{\max}$ measured by a PIP disdrometer at Hurricane Ridge for snow events during (left) prefrontal and (right) postfrontal cases.

downstream over the high terrain and lee side. This often results in equal or greater precipitation rates on the lee slopes than upstream at the coast (Fig. 12b). Although the PSDs varied by case, the precipitation rate at Hurricane Ridge was close to 3 mm h$^{-1}$ in all three warm sectors (Table 4). While some case-to-case variability exists in PSDs at Hurricane Ridge, the degree of variability is far less than the windward locations that appear to be more strongly influenced by warm precipitation processes.

Another notable feature of Figs. 10c, 10d, and 15 is the smaller $D_o$ and remarkably high $N_w$ on 13 November that is present to an extent at all three ground sites, suggesting large concentrations of small raindrops that were likely produced by warm precipitation processes (Zagrodnik et al. 2018). Several pieces of evidence suggest that warm precipitation processes were dominant in this case. The consistently small $D_o$ and high $N_w$ at the Fishery site (Figs. 10c,d) indicates a lack of contribution from stratiform rain forced by the synoptic system, which produces PSDs closer to those observed in the prefrontal sector (Figs. 10a,b). Additionally, the 15-dB$Z$ echo-top height was the lowest of the three warm-sector cases over the ocean, coast, windward side, and high terrain (not shown).[1] Despite the apparent lack of ice processes, this case experienced the highest precipitation rates of any case in this study (Table 4).

[1] The DC-8 did not fly over the lee side on 13 November.

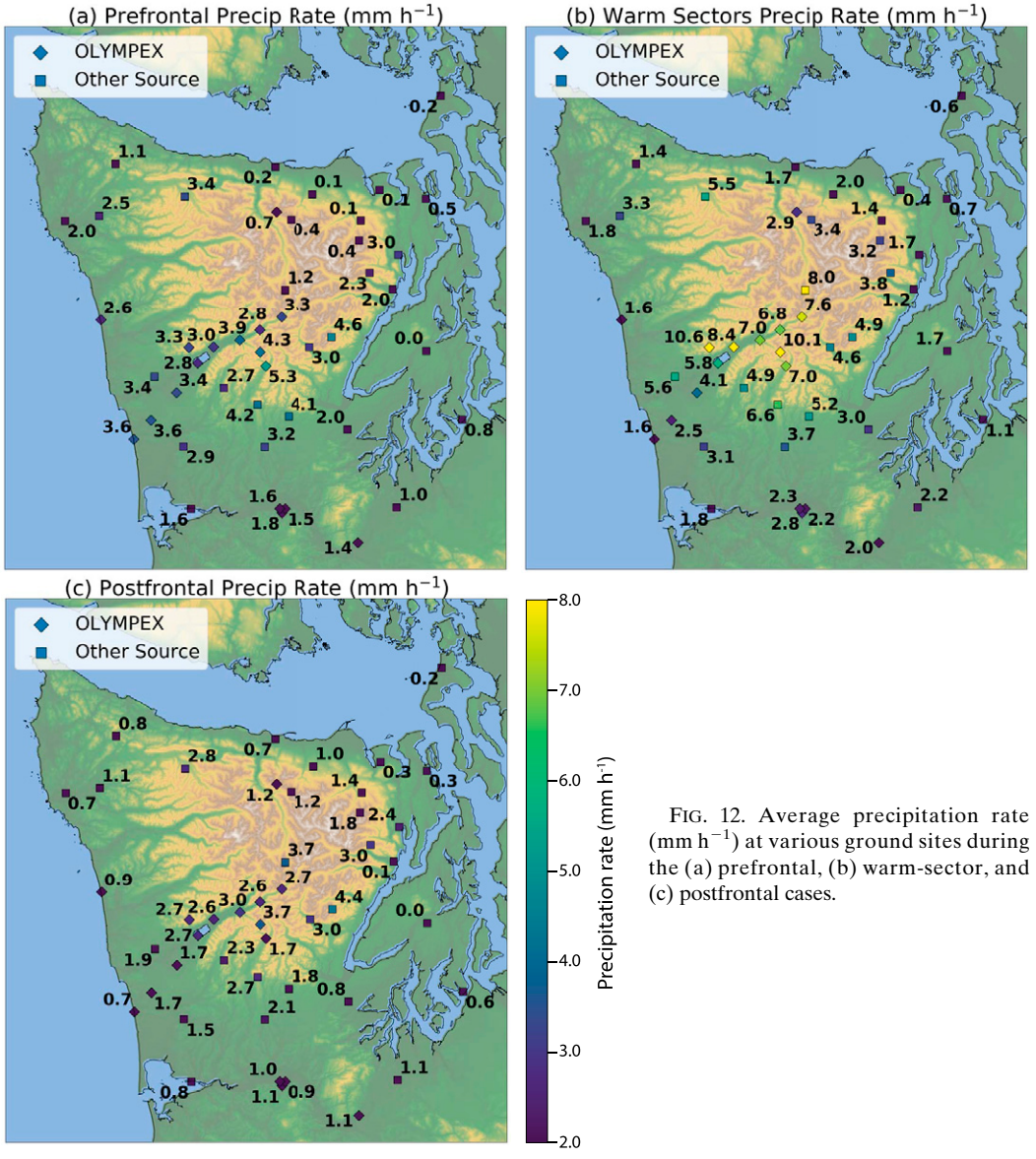


FIG. 12. Average precipitation rate (mm h$^{-1}$) at various ground sites during the (a) prefrontal, (b) warm-sector, and (c) postfrontal cases.

*c. Postfrontal*

1) RADAR

Figure 6e shows an example of how the postfrontal precipitation structures differ from the other storm sectors. Over the ocean the aircraft observed a shallow, isolated convective cell with a convective core extending only to about 3-km height. The plan position indicator (PPI) image (Fig. 6f) shows that this cell was near the edge of a broad region of isolated convective showers. At the coast, the precipitation was more stratiform in nature with a well-defined bright band and stronger echoes remaining relatively shallow. Over terrain, the echoes were broader and somewhat deeper but also horizontally heterogeneous, suggesting a mix of convective- and stratiform-type precipitation with some embedded updrafts.

The postfrontal CFADs in Fig. 16 also have different shapes than both the prefrontal and warm-sector CFADs. The concentration of the modal contours in the lower levels indicates that postfrontal precipitation is generally shallower and more convective in nature than other storm sectors. Postfrontal echo over the ocean was generally weak, 10–20 dB$Z$, although it occasionally reached 30–40 dB$Z$ in isolated convective cores below 2 km.

As the postfrontal precipitation moved from ocean to coast to the windward to the high terrain (Figs. 16b–e),

TABLE 4. Average precipitation rate (mm h$^{-1}$) at the three disdrometer sites (see Fig. 2 for locations) for the nine cases described in this study.

| Case | Category | Fishery rain rate (mm h$^{-1}$) | Prairie Creek rain rate (mm h$^{-1}$) | Hurricane Ridge rain rate (mm h$^{-1}$) |
|---|---|---|---|---|
| 1–2 Dec 2015 | Prefrontal | 1.5 | 3.3 | 0.2 |
| 5 Dec 2015 | Prefrontal | 3.5 | 3.1 | 1.0 |
| 12 Dec 2015 | Prefrontal | 3.6 | 3.6 | 0.7 |
| 13 Nov 2015 | Warm sector | 6.2 | 14.1 | 3.1 |
| 3 Dec 2015 | Warm sector | 2.7 | 3.0 | 3.3 |
| 8 Dec 2015 | Warm sector | 4.0 | 13.1 | 3.1 |
| 4 Dec 2015 | Postfrontal | 0.6 | 0.5 | 0.1 |
| 10 Dec 2015 | Postfrontal | 2.7 | 2.7 | 1.8 |
| 13 Dec 2015 | Postfrontal | 1.7 | 3.7 | 1.1 |

the modal distribution in the CFADs narrowed and shifted downward and to the right. The high-terrain distribution in particular was dominated by 20–30-dB$Z$ echo below 4 km and very little corresponding echo at higher levels. Compared to the stratiform-dominated prefrontal CFADs (Fig. 7), the postfrontal high-terrain CFAD had a much higher occurrence of echoes >20 dB$Z$ above the bright band (located below the 1.5-km bottom of the postfrontal CFADs; Table 3), suggesting strong but shallow upward motion and robust ice production. Figures 9e and 9f confirm that the precipitation broadens in coverage but does not appreciably deepen over terrain. The 15-dB$Z$ echo tops reached a similar height on average over the ocean, coast, windward, and high terrain, while the 15-dB$Z$ echo coverage more than doubled from the ocean to the high terrain.

These statistics suggest that isolated postfrontal convective showers undergo a transition to broader, more

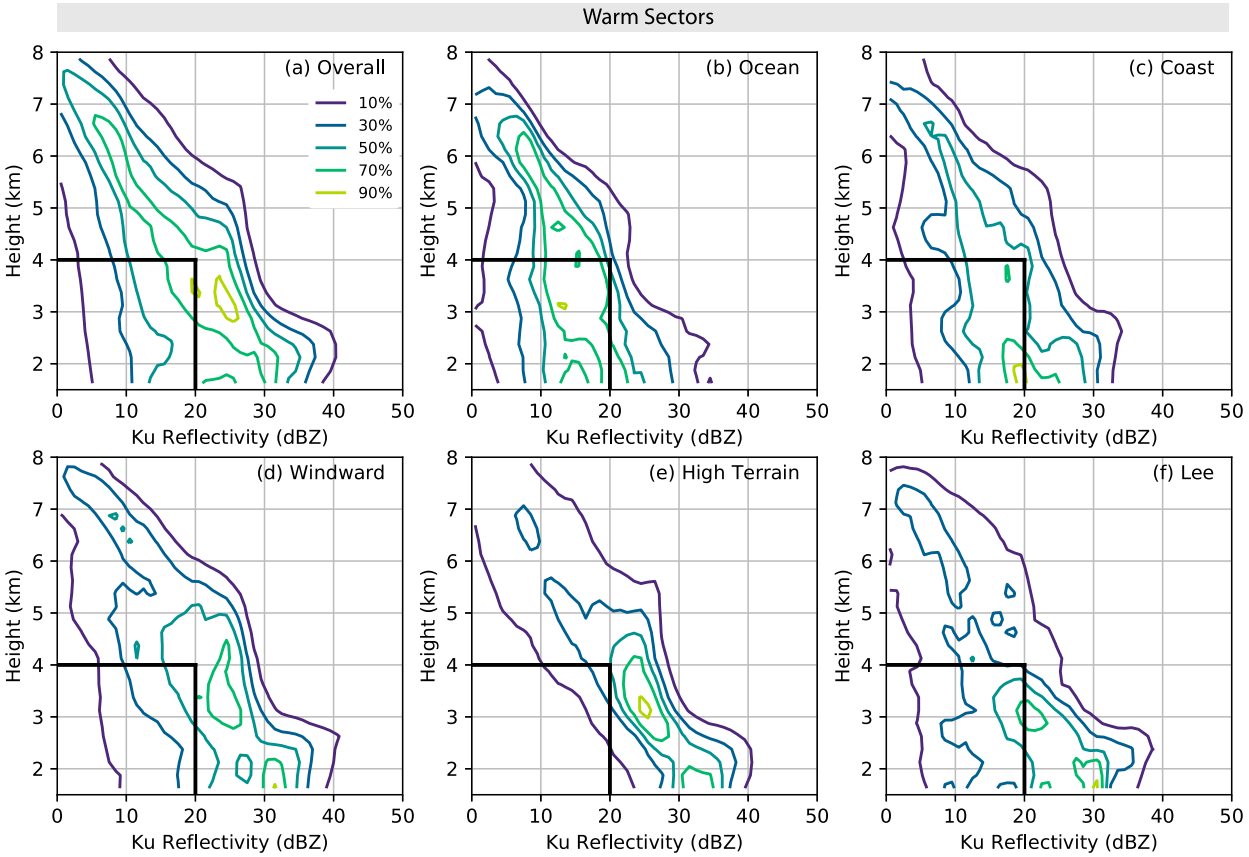


FIG. 13. As in Fig. 7, but for warm-sector cases.

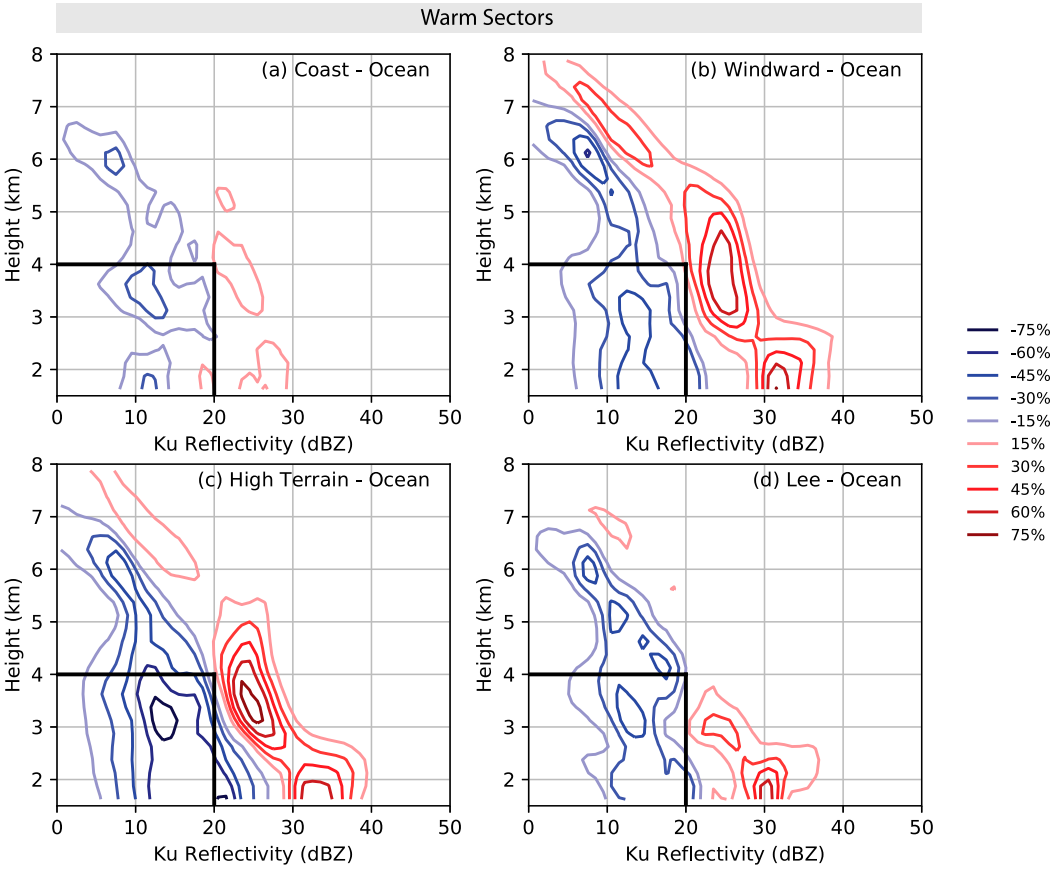


FIG. 14. As in Fig. 8, but for warm-sector cases.

stratiform-like nature as they move from the ocean to the high terrain of the Olympic Mountains. There are several potential reasons why postfrontal precipitation changes in character over land: 1) different surface sensible and latent heat fluxes between ocean and land (Bond and Fleagle 1988; Sikora et al. 2011), 2) the widespread release of conditional instability as the cells encounter complex terrain (Fig. 5), and 3) widespread orographic lifting of near moist-neutral air following release of instability produces stratiform cloud and precipitation between active convective elements (Cannon et al. 2012). The moist static stability profiles in Fig. 5 show that conditional instability is concentrated in the lowest 1.5 km and the profiles are nearly moist neutral above 1.5 km. In this environment it is not surprising that the postfrontal enhancement of

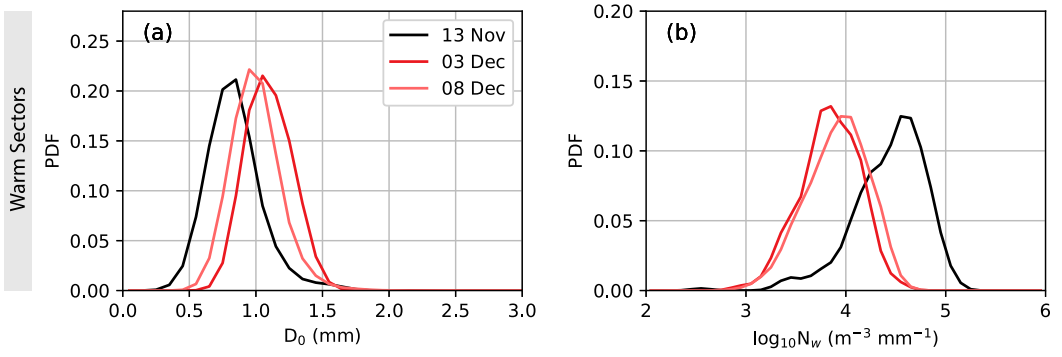


FIG. 15. Histograms of 1-min (a) $D_o$ and (b) $N_w$ measured at Hurricane Ridge during rain events for warm-sector cases.

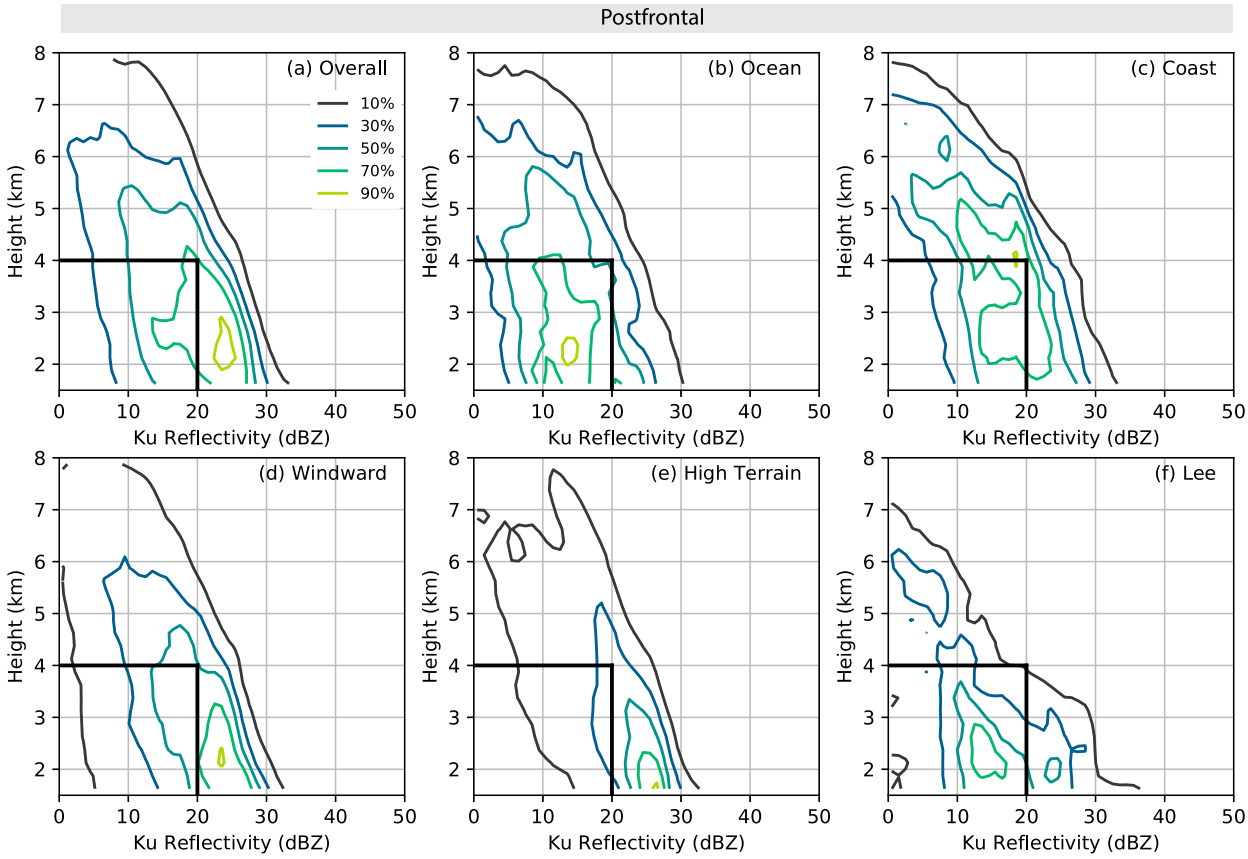


FIG. 16. As in Fig. 7, but for postfrontal cases.

reflectivity over terrain (Figs. 17a–c) occurs mostly below 3 km. The slightly deeper enhancement at the coast (Fig. 17a) may be a sampling artifact due to the more isolated nature of postfrontal cells upstream of terrain.

As in other storm sectors, precipitation intensity declines over the lee side in the postfrontal sector. The leeside CFAD (Fig. 16f) and difference CFAD (Fig. 17d) shows weakened echo above 3 km relative to the ocean. Figures 9e and 9f show a corresponding reduction in 15-dB$Z$ echo height and reduced coverage on the north and northeast portion of the Olympic Mountains. Some of the precipitation in the leeside CFAD is a result of westerly component large-scale flow (Fig. 4c) during two of the three postfrontal cases. In those cases, the northern side of the Olympic Mountains was not the truly the lee side. Westerly flow allowed shallow postfrontal cells to move eastward through the Strait of Juan de Fuca rather than transecting the Olympic Mountains. Still, the reduced precipitation rates on the northern and northeastern side of the high terrain including at Hurricane Ridge (Fig. 12c) indicates that postfrontal precipitation that does transect the mountains eventually weakens as it approaches the lee side, where downward motion occurs aloft.

### 2) PRECIPITATION CHARACTERISTICS

Figures 10e and 10f show that all three of the postfrontal cases exhibited broad histograms of $D_o$ and $N_w$ at both Fishery and Prairie Creek, although $N_w$ did not reach as high as two of the warm-sector cases. The similarity between the two sites is unsurprising given the postfrontal rain rate was only 1 mm h$^{-1}$ higher at Prairie Creek than Fishery (Fig. 12c). Most of the enhancement between Fishery and Prairie Creek occurred on 13 December (Table 4) and it was mostly a result of larger $D_o$. The broad distributions are a consequence of the convective nature of postfrontal precipitation, a property that is mostly retained at the windward Prairie Creek site despite a somewhat narrower CFAD distribution in Fig. 16d.

The Hurricane Ridge snow parameter histograms in Figs. 11b, 11d, and 11f are also fairly broad, although not appreciably more so than for the prefrontal sector. The 4 December case had some very light precipitation that may have included blowing snow (discussed

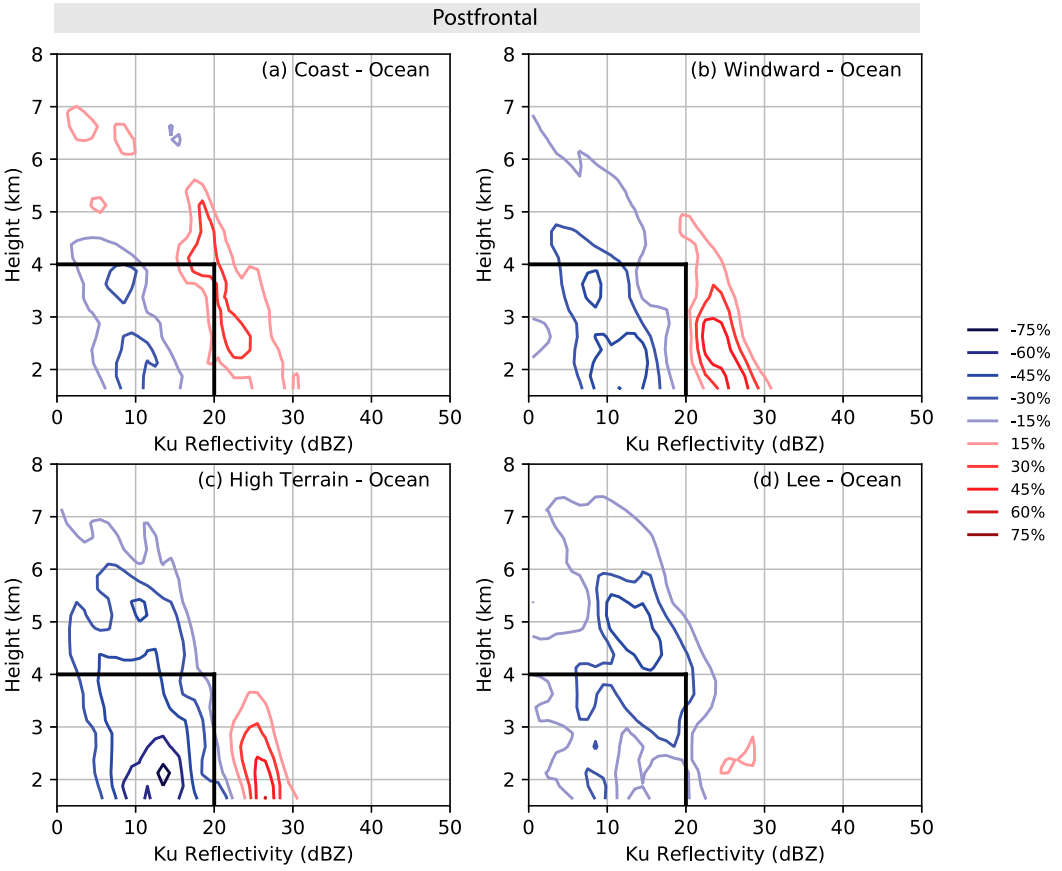


FIG. 17. As in Fig. 8, but for postfrontal cases.

in section 2b). The $D_o$ modes were all around 2.5–3.0 mm. Particle concentrations were fairly high but not beyond what was observed in the prefrontal sector (Fig. 10f). The most notable aspect of the postfrontal disdrometer measurements is that all three cases recorded numerous aggregates with diameters of 10–15+ mm, especially 13 December which had a mode above 10 mm. Figure 12c shows that the average postfrontal precipitation rates increased from $<1\,\text{mm h}^{-1}$ at the coast to $2–4\,\text{mm h}^{-1}$ over the windward slopes and gradually decreased down to $0–2\,\text{mm h}^{-1}$ over the high terrain and lee side. While the precipitation rates over the high terrain were modest, the low melting levels and the long duration of some of the postfrontal periods resulted in significant snow accumulation over the high terrain during OLYMPEX.

## 5. Conclusions

This study has examined airborne precipitation radar data, surface precipitation measurements, and particle size distributions from nine storms passing over the three-dimensional (dome shaped) Olympic Mountain range during the OLYMPEX field campaign. The prefrontal, warm sectors, and postfrontal events had distinct synoptic-scale environmental conditions as reflected in sounding-derived wind and moist static stability profiles (see section 3 and Figs. 4 and 5). Consistent with Zagrodnik et al. (2018) and PK18, the differing synoptic-scale conditions were related to storm sectors. The degree of windward enhancement and leeside diminishment of precipitation, though always present, varied considerably from case to case. The dynamical and microphysical mechanisms by which the preexisting precipitation was modified by terrain depended on the airflow and stability properties of the incoming air mass and nature of the preexisting precipitation forced by the frontal cyclone prior to landfall. We documented the following processes in each storm sector.

### *a. Prefrontal*

Prefrontal precipitation contained a predominance of a uniform, mature stratiform echo both over ocean and over terrain with little time variance in reflectivity and particle size distributions on the windward side of

the barrier. Deeper echoes and modest enhancement of midlevel reflectivity were observed over the windward slopes along with a corresponding slight increase in precipitation totals. The stably stratified prefrontal storm environment encouraged midlevel lifting upstream of the barrier near the coast and suppressed low-level lift on the windward slopes. Echo tops declined beginning over the high terrain and low-level reflectivity diminished considerably in the lee, resulting in a nearly complete rain shadow on the northeast side of the Olympic Mountains.

### b. Warm sectors

Warm sectors featured deep and intense enhancement of reflectivity above, within, and below the melting level over both the windward slopes and high terrain. The composition and intensity of warm-sector precipitation was not uniform but rather was highly variable both in the upstream clouds over the ocean and on the windward slopes. The two cases where the low-level flow aligned with the southwest-facing Quinault valley resulted in the greatest enhancement of precipitation on the lower-windward slopes, consistent with descriptions of atmospheric rivers by Neiman et al. (2017) and Zagrodnik et al. (2018). Warm precipitation processes made an appreciable contribution to the enhancement, as evidenced by PSDs favoring high drop concentrations (high $N_w$) in the two cases with southwesterly flow. In contrast to prefrontal periods, even the leeside precipitation was enhanced within and below the bright band, suggesting a spillover of frozen hydrometeors from higher levels over the windward side and high terrain. The spillover was facilitated by strong cross-barrier winds advecting ice particles that were produced upstream over terrain possibly from enhanced ice particle growth within the secondary reflectivity maximum at 4–5 km. Particle size data at Hurricane Ridge showed that the advected precipitation was rather homogeneous and lacked the undulations in particle size and concentration that occurred at the windward sites.

### c. Postfrontal

Postfrontal precipitation was predominantly isolated and convective in nature over ocean. Over land, it transitioned to a broader and more widespread stratiform echo while retaining intense cores, characteristic of embedded convection. The surface rain and snow particle size distributions were correspondingly variable, consistent with the precipitation being a mixture of convective and stratiform. Precipitation totals were enhanced on the windward side and over the high terrain and diminished on the lee side, although moisture flowing from west to east through the Strait of Juan de Fuca appeared to reduce the degree to which the echo was diminished below 3 km.

### d. Implications

The enhancement of rain on the windward sides and drying on lee sides of West Coastal mountain ranges are of utmost importance for hydrologic, climatic, and weather forecasting applications. The results of this study show how the processes controlling the pattern of enhancement and diminishment of precipitation over a nearly circular three-dimensional coastal mountain barrier is highly sensitive to synoptic-scale properties of landfalling frontal cyclones. The OLYMPEX cases described in this study and in PK18 exhibit stronger rain shadows in the prefrontal period and weaker rain shadows in warm sectors. The dome shape of the Olympic Mountains is not conductive to prefrontal cold-air trapping in the lee, allowing for descent and corresponding diminishment of echo in the lower levels of the lee (Figs. 6a and 7a). This study suggests that outside of the postfrontal sector, an important mechanism producing leeside precipitation is downstream spillover of ice particles formed in deep clouds directly over the Olympic Mountains. The degree of diminishment on the lee side of the three-dimensional range is thus partially controlled by the synoptic-scale processes conducive to producing such spillover.

On the windward side, OLYMPEX data show that varying contributions of liquid- and ice-phase microphysical processes between storm sectors and geographic regions are responsible for the observed precipitation patterns (Zagrodnik et al. 2018). Model simulations in PK18 required ''seeding'' by background precipitation of at least 0.5 mm $h^{-1}$ to sufficiently enhance precipitation over the windward slopes. OLYMPEX ground-based data in warm sectors show that upstream precipitation at the coast largely exceeded this rate (Fig. 12b). However, the relatively small median particle sizes observed during warm sectors (Fig. 10c) indicate that growth by collection of cloud water by ice particles is not necessarily the dominant enhancement mechanism. Rather, the consistently high drop concentrations on the lower windward slopes (Fig. 10d) suggest that warm rain processes make a significant contribution to the high precipitation rates observed upstream of the interior high terrain. It follows that the complexity and variability of precipitation over the Olympic Mountains is not adequately explained by paradigms such as the ''seeder–feeder'' mechanism (Bergeron 1968) or bifurcation into brightband and nonbrightband rain (White et al. 2003). Lifting over complex terrain modifies both the lower-level warm processes and the upper-level ice processes, often concurrently. The lifting

over the terrain moreover varies with the differences in synoptic/dynamic conditions in different storm sectors. Different precipitation patterns result depending on which processes are dominant in the portion of the synoptic-scale storm passing over the mountains.

*Acknowledgments.* The authors would also like to thank the Olympic National Park staff, the U.S. Forest Service staff, and the Quinault Indian Nation for permission to install instrumentation on their land. Randy Chase provided code and guidance for interpreting the APR-3 dataset. Bill Baccus, Dave Wolff, Matt Wingo, Dr. Ali Tokay, Dr. Patrick Gatlin, and Dr. Larry Bliven contributed to the collection and interpretation of surface observations. A Colorado State University team lead by Dr. Paul Ciesielski launched soundings and performed quality-control procedures. Comments from three anonymous reviewers considerably strengthened the manuscript. This research was supported by NASA Grants NNX16AD75G and 80NSSC17K0279 and NSF Grants AGS-1503155 and AGS-1657251. Part of this research was carried out at the Jet Propulsion Laboratory, California Institute of Technology, under a contract with the National Aeronautics and Space Administration.

## REFERENCES

Anders, A. M., G. H. Roe, D. R. Durran, and J. R. Minder, 2007: Small-scale spatial gradients in climatological precipitation on the Olympic Peninsula. *J. Hydrometeor.*, **8**, 1068–1081, https://doi.org/10.1175/JHM610.1.

Atlas, D., R. C. Srivastava, and R. S. Sekhon, 1973: Doppler radar characteristics of precipitation at vertical incidence. *Rev. Geophys.*, **11**, 1–35, https://doi.org/10.1029/RG011i001p00001.

Barrett, B. S., R. D. Garreaud, and M. Falvey, 2009: Effect of the Andes Cordillera on precipitation from a midlatitude cold front. *Mon. Wea. Rev.*, **137**, 3092–3109, https://doi.org/10.1175/2009MWR2881.1.

Bergeron, T., 1968: Studies of the orogenic effect on the areal fine structure of rainfall distribution. Uppsala University Meteorological Institute Rep. 6, 42 pp.

Bond, N. A., and R. G. Fleagle, 1988: Prefrontal and postfrontal boundary layer processes over the ocean. *Mon. Wea. Rev.*, **116**, 1257–1273, https://doi.org/10.1175/1520-0493(1988)116<1257:PAPBLP>2.0.CO;2.

——, and Coauthors, 1997: The Coastal Observation and Simulation with Topography (COAST) experiment. *Bull. Amer. Meteor. Soc.*, **78**, 1941–1955, https://doi.org/10.1175/1520-0477(1997)078<1941:TCOASW>2.0.CO;2.

Cannon, D. J., D. J. Kirshbaum, and S. L. Gray, 2012: Under what conditions does embedded convection enhance orographic precipitation? *Quart. J. Roy. Meteor. Soc.*, **138**, 391–406, https://doi.org/10.1002/qj.926.

Chase, R. J., and Coauthors, 2018: Evaluation of triple-frequency radar retrieval of snowfall properties using coincident airborne in-situ observations during OLYMPEX. *Geophys. Res. Lett.*, **45**, 5752–5760, https://doi.org/10.1029/2018GL077997.

Ciesielski, P. E., and Coauthors, 2014: Quality-controlled upper-air sounding dataset for DYNAMO/CINDY/AMIE: Development and corrections. *J. Atmos. Oceanic Technol.*, **31**, 741–764, https://doi.org/10.1175/JTECH-D-13-00165.1.

Colle, B. A., 2004: Sensitivity of orographic precipitation to changing ambient conditions and terrain geometries: An idealized modeling perspective. *J. Atmos. Sci.*, **61**, 588–606, https://doi.org/10.1175/1520-0469(2004)061<0588:SOOPTC>2.0.CO;2.

——, and C. F. Mass, 1996: An observational and modeling study of the interaction of low-level southwesterly flow with the Olympic Mountains during COAST IOP 4. *Mon. Wea. Rev.*, **124**, 2152–2175, https://doi.org/10.1175/1520-0493(1996)124<2152:AOAMSO>2.0.CO;2.

Daly, C., M. Halbleib, J. I. Smith, W. P. Gibson, M. K. Doggett, G. H. Taylor, J. Curtis, and P. P. Pasteris, 2008: Physiographically sensitive mapping of climatological temperature and precipitation across the conterminous United States. *Int. J. Climatol.*, **28**, 2031–2064, https://doi.org/10.1002/joc.1688.

Durden, S. L., and S. Tanelli, 2018: GPM ground validation Airborne Precipitation Radar 3rd Generation (APR-3) OLYMPEX, version 2. NASA Global Hydrology Center DAAC, accessed 8 May 2018, https://doi.org/10.5067/GPMGV/OLYMPEX/APR3/DATA201.

Durran, D. R., 1990: Mountain waves and downslope winds. *Atmospheric Processes over Complex Terrain*, *Meteor. Monogr.*, No. 23, Amer. Meteor. Soc., 59–81, http://link.springer.com/10.1007/978-1-935704-25-6_4.

——, and J. B. Klemp, 1982: On the effects of moisture on the Brunt–Väisälä frequency. *J. Atmos. Sci.*, **39**, 2152–2158, https://doi.org/10.1175/1520-0469(1982)039<2152:OTEOMO>2.0.CO;2.

Hardin, J., and N. Guy, 2017: PyDisdrometer Version 1.0. Zenodo, http://doi.org/10.5281/zenodo.9991.

Hecht, C. W., and J. M. Cordeira, 2017: Characterizing the influence of atmospheric river orientation and intensity on precipitation distributions over north coastal California. *Geophys. Res. Lett.*, **44**, 9048–9058, https://doi.org/10.1002/2017GL074179.

Hobbs, P. V., 1978: Organization and structure of clouds and precipitation on the mesoscale and microscale in cyclonic storms. *Rev. Geophys.*, **16**, 741–755, https://doi.org/10.1029/RG016i004p00741.

——, and Coauthors, 1971: Studies of winter cyclonic storms over the Cascade Mountains (1970–71). University of Washington Dept. of Atmospheric Sciences Cloud Physics Group Research Rep. VI, 306 pp., http://carg.atmos.washington.edu/sys/research/archive/winter_cyclonic.pdf.

——, R. C. Easter, and A. B. Fraser, 1973: A theoretical study of the flow of air and fallout of solid precipitation over mountainous terrain: Part II. Microphysics. *J. Atmos. Sci.*, **30**, 813–823, https://doi.org/10.1175/1520-0469(1973)030<0813:ATSOTF>2.0.CO;2.

Horel, J., and Coauthors, 2002: MesoWest: Cooperative mesonets in the western United States. *Bull. Amer. Meteor. Soc.*, **83**, 211–225, https://doi.org/10.1175/1520-0477(2002)083<0211:MCMITW>2.3.CO;2.

Houze, R. A., Jr., 2014: *Cloud Dynamics*. 2nd ed. Elsevier, 432 pp.

——, and P. V. Hobbs, 1982: Organization and structure of precipitating cloud systems. *Adv. Geophys.*, **24**, 225–300, https://doi.org/10.1016/S0065-2687(08)60521-X.

——, and S. Medina, 2005: Turbulence as a mechanism for orographic precipitation enhancement. *J. Atmos. Sci.*, **62**, 3599–3623, https://doi.org/10.1175/JAS3555.1.

——, J. D. Locatelli, and P. V. Hobbs, 1976: Dynamics and cloud microphysics of the rainbands in an occluded frontal system.

*J. Atmos. Sci.*, **33**, 1921–1936, https://doi.org/10.1175/1520-0469(1976)033<1921:DACMOT>2.0.CO;2.

——, C. N. James, and S. Medina, 2001: Radar observations of precipitation and airflow on the Mediterranean side of the Alps: Autumn 1998 and 1999. *Quart. J. Roy. Meteor. Soc.*, **127**, 2537–2558, https://doi.org/10.1002/qj.49712757804.

——, and Coauthors, 2017: The Olympic Mountains Experiment (OLYMPEX). *Bull. Amer. Meteor. Soc.*, **98**, 2167–2188, https://doi.org/10.1175/BAMS-D-16-0182.1.

James, C. N., and R. A. Houze, 2005: Modification of precipitation by coastal orography in storms crossing Northern California. *Mon. Wea. Rev.*, **133**, 3110–3131, https://doi.org/10.1175/MWR3019.1.

Kingsmill, D. E., P. J. Neiman, F. M. Ralph, and A. B. White, 2006: Synoptic and topographic variability of Northern California precipitation characteristics in landfalling winter storms observed during CALJET. *Mon. Wea. Rev.*, **134**, 2072–2094, https://doi.org/10.1175/MWR3166.1.

Mass, C. F., and G. K. Ferber, 1990: Surface pressure perturbations produced by an isolated mesoscale topographic barrier. Part I: General characteristics and dynamics. *Mon. Wea. Rev.*, **118**, 2579–2596, https://doi.org/10.1175/1520-0493(1990)118<2579:SPPPBA>2.0.CO;2.

——, N. Johnson, M. Warner, and R. Vargas, 2015: Synoptic control of cross-barrier precipitation ratios for the Cascade Mountains. *J. Hydrometeor.*, **16**, 1014–1028, https://doi.org/10.1175/JHM-D-14-0149.1.

Massmann, A. K., J. R. Minder, R. D. Garreaud, D. E. Kingsmill, R. A. Valenzuela, A. Montecinos, S. L. Fults, and J. R. Snider, 2017: The Chilean Coastal Orographic Precipitation Experiment: Observing the influence of microphysical rain regimes on coastal orographic precipitation. *J. Hydrometeor.*, **18**, 2723–2743, https://doi.org/10.1175/JHM-D-17-0005.1.

Matejka, T. J., R. A. Houze Jr., and P. V. Hobbs, 1980: Microphysics and dynamics of clouds associated with mesoscale rainbands in extratropical cyclones. *Quart. J. Roy. Meteor. Soc.*, **106**, 29–56, https://doi.org/10.1002/qj.49710644704.

McMurdie, L. A., A. K. Rowe, R. A. Houze Jr., S. R. Brodzik, J. P. Zagrodnik, and T. M. Schuldt, 2018: Terrain-enhanced precipitation processes above the melting layer: Results from OLYMPEX. *J. Geophys. Res. Atmos.*, **123**, 12 194–12 209, https://doi.org/10.1029/2018JD029161.

Medina, S., E. Sukovich, and R. A. Houze Jr., 2007: Vertical structures of precipitation in cyclones crossing the Oregon Cascades. *Mon. Wea. Rev.*, **135**, 3565–3586, https://doi.org/10.1175/MWR3470.1.

Minder, J. R., D. R. Durran, G. H. Roe, and A. M. Anders, 2008: The climatology of small-scale orographic precipitation over the Olympic Mountains: Patterns and processes. *Quart. J. Roy. Meteor. Soc.*, **134**, 817–839, https://doi.org/10.1002/qj.258.

——, ——, and ——, 2011: Mesoscale controls on the mountain-side snow line. *J. Atmos. Sci.*, **68**, 2107–2127, https://doi.org/10.1175/JAS-D-10-05006.1.

Nagle, R. E., and S. M. Serebreny, 1962: Radar precipitation echo and satellite cloud observations of a maritime cyclone. *J. Appl. Meteor.*, **1**, 279–295, https://doi.org/10.1175/1520-0450(1962)001<0279:RPEASC>2.0.CO;2.

Neiman, P. J., L. J. Schick, F. M. Ralph, M. Hughes, and G. A. Wick, 2011: Flooding in western Washington: The connection to atmospheric rivers. *J. Hydrometeor.*, **12**, 1337–1358, https://doi.org/10.1175/2011JHM1358.1.

——, and Coauthors, 2017: An analysis of coordinated observations from NOAA's *Ronald H. Brown* ship and G-IV aircraft in a landfalling atmospheric river over the North Pacific during CalWater-2015. *Mon. Wea. Rev.*, **145**, 3647–3669, https://doi.org/10.1175/MWR-D-17-0055.1.

Newman, A. J., P. A. Kucera, and L. F. Bliven, 2009: Presenting the Snowflake Video Imager (SVI). *J. Atmos. Oceanic Technol.*, **26**, 167–179, https://doi.org/10.1175/2008JTECHA1148.1.

NWAC, 2018: Northwest Avalanche Center weather station data portal—Olympics region, continuing from 2014 (updated daily). Northwest Avalanche Center, accessed 23 April 2018, https://www.nwac.us/data-portal/location/hurricane-ridge/.

Petersen, W. A., D. Wolff, J. Wang, and A. Tokay, 2017a: GPM ground validation Met One rain gauge pairs OLYMPEX. NASA Global Hydrology Center DAAC. Subset used: All sites, November–December 2015, accessed 23 April 2018, https://doi.org/10.5067/GPMGV/OLYMPEX/GAUGES/DATA201.

——, A. Tokay, and P. N. Gatlin, 2017b: GPM ground validation Pluvio precipitation gauges OLYMPEX. NASA Global Hydrology Center DAAC. Subset used: Wynoochee site, November–December 2015, accessed 23 April 2018, https://doi.org/10.5067/GPMGV/OLYMPEX/PLUVIO/DATA301.

——, ——, ——, and M. T. Wingo, 2017c: GPM ground validation Autonomous Parsivel Unit (APU) OLYMPEX. NASA Global Hydrology Center DAAC. Subset used: APU03 and APU06, November–December 2015, accessed 28 March 2018, https://doi.org/10.5067/GPMGV/OLYMPEX/APU/DATA301.

Picard, L., and C. Mass, 2017: The sensitivity of orographic precipitation to flow direction: An idealized modeling approach. *J. Hydrometeor.*, **18**, 1673–1688, https://doi.org/10.1175/JHM-D-16-0209.1.

Purnell, D. J., and D. J. Kirshbaum, 2018: Synoptic control over orographic precipitation distributions during the Olympics Mountains Experiment (OLYMPEX). *Mon. Wea. Rev.*, **146**, 1023–1044, https://doi.org/10.1175/MWR-D-17-0267.1.

Ralph, F. M., and Coauthors, 1999: The California Land-Falling Jets Experiment (CALJET): Objectives and design of a coastal atmosphere–ocean observing system deployed during a strong El Niño. Preprints, *Third Symp. on Integrated Observing Systems*, Dallas, TX, Amer. Meteor. Soc., 78–81.

——, P. J. Neiman, and G. A. Wick, 2004: Satellite and CALJET aircraft observations of atmospheric rivers over the eastern North Pacific Ocean during the winter of 1997/98. *Mon. Wea. Rev.*, **132**, 1721–1745, https://doi.org/10.1175/1520-0493(2004)132<1721:SACAOO>2.0.CO;2.

Sikora, T. D., G. S. Young, C. M. Fisher, and M. D. Stepp, 2011: A synthetic aperture radar–based climatology of open-cell convection over the northeast Pacific Ocean. *J. Appl. Meteor. Climatol.*, **50**, 594–603, https://doi.org/10.1175/2010JAMC2624.1.

Siler, N., and D. Durran, 2016: What causes weak orographic rain shadows? Insights from case studies in the Cascades and idealized simulations. *J. Atmos. Sci.*, **73**, 4077–4099, https://doi.org/10.1175/JAS-D-15-0371.1.

Skofronick-Jackson, G., and Coauthors, 2017: The Global Precipitation Measurement (GPM) mission for science and society. *Bull. Amer. Meteor. Soc.*, **98**, 1679–1695, https://doi.org/10.1175/BAMS-D-15-00306.1.

Smith, R. B., and I. Barstad, 2004: A linear theory of orographic precipitation. *J. Atmos. Sci.*, **61**, 1377–1391, https://doi.org/10.1175/1520-0469(2004)061<1377:ALTOOP>2.0.CO;2.

Stoelinga, M. T., and Coauthors, 2003: Improvement of microphysical parameterization through observational verification experiment. *Bull. Amer. Meteor. Soc.*, **84**, 1807–1826, https://doi.org/10.1175/BAMS-84-12-1807.

Testud, J., S. Oury, R. A. Black, P. Amayenc, and X. Dou, 2001: The concept of ''normalized'' distribution to describe raindrop spectra: A tool for cloud physics and cloud remote sensing. *J. Appl. Meteor.*, **40**, 1118–1140, https://doi.org/10.1175/1520-0450(2001)040<1118:TCONDT>2.0.CO;2.

Thompson, E. J., S. A. Rutledge, B. Dolan, and M. Thurai, 2015: Drop size distributions and radar observations of convective and stratiform rain over the equatorial Indian and west Pacific Oceans. *J. Atmos. Sci.*, **72**, 4091–4125, https://doi.org/10.1175/JAS-D-14-0206.1.

Tokay, A., D. B. Wolff, and W. A. Petersen, 2014: Evaluation of the new version of the laser-optical disdrometer, OTT Parsivel 2. *J. Atmos. Oceanic Technol.*, **31**, 1276–1288, https://doi.org/10.1175/JTECH-D-13-00174.1.

Viale, M., K. L. Rasmussen, and R. A. Houze Jr., 2013: Upstream orographic enhancement of a narrow cold-frontal rainband approaching the Andes. *Mon. Wea. Rev.*, **141**, 1708–1730, https://doi.org/10.1175/MWR-D-12-00138.1.

von Lerber, A., D. Moisseev, L. F. Bliven, W. Petersen, A.-M. Harri, and V. Chandrasekar, 2017: Microphysical properties of snow and their link to $Z_e$–$S$ relations during BAECC 2014. *J. Appl. Meteor. Climatol.*, **56**, 1561–1582, https://doi.org/10.1175/JAMC-D-16-0379.1.

——, ——, D. A. Marks, W. Petersen, A.-M. Harri, and V. Chandrasekar, 2018: Validation of GMI snowfall observations by using a combination of weather radar and surface measurements. *J. Appl. Meteor. Climatol.*, **57**, 797–820, https://doi.org/10.1175/JAMC-D-17-0176.1.

White, A. B., P. J. Neiman, F. M. Ralph, D. E. Kingsmill, and P. O. G. Persson, 2003: Coastal orographic rainfall processes observed by radar during the California Land-Falling Jets Experiment. *J. Hydrometeor.*, **4**, 264–282, https://doi.org/10.1175/1525-7541(2003)4<264:CORPOB>2.0.CO;2.

Yuter, S. E., and R. A. Houze, 1995: Three-dimensional kinematic and microphysical evolution of Florida cumulonimbus. Part II: Frequency distributions of vertical velocity, reflectivity, and differential reflectivity. *Mon. Wea. Rev.*, **123**, 1941–1963, https://doi.org/10.1175/1520-0493(1995)123<1941:TDKAME>2.0.CO;2.

Zagrodnik, J. P., L. A. McMurdie, and R. A. Houze, 2018: Stratiform precipitation processes in cyclones passing over a coastal mountain range. *J. Atmos. Sci.*, **75**, 983–1004, https://doi.org/10.1175/JAS-D-17-0168.1.

Zängl, G., 2005: The impact of lee-side stratification on the spatial distribution of orographic precipitation. *Quart. J. Roy. Meteor. Soc.*, **131**, 1075–1091, https://doi.org/10.1256/qj.04.118.